Advances in Mixed Tin-Lead Narrow-Bandgap Perovskites for Single-Junction and All-Perovskite Tandem Solar Cells

*Fengjiu Yang and Kai Zhu**

Organic–inorganic metal-halide perovskites have received great attention for photovoltaic (PV) applications owing to their superior optoelectronic properties and the unprecedented performance development. For single-junction PV devices, although lead (Pb)-based perovskite solar cells have achieved 26.1% efficiency, the mixed tin-lead (Sn-Pb) perovskites offer more ideal bandgap tuning capability to enable an even higher performance. The Sn-Pb perovskite (with a bandgap tuned to ≈1.2 eV) is also attractive as the bottom subcell for a tandem configuration to further surpass the Shockley–Queisser radiative limit for the single-junction devices. The performance of the all-perovskite tandem solar cells has gained rapid development and achieved a certified efficiency up to 29.1%. In this article, the properties and recent development of state-of-the-art mixed Sn-Pb perovskites and their application in single-junction and all-perovskite tandem solar cells are reviewed. Recent advances in various approaches covering additives, solvents, interfaces, and perovskite growth are highlighted. The authors also provide the perspective and outlook on the challenges and strategies for further development of mixed Sn-Pb perovskites in both efficiency and stability for PV applications.

1. Introduction

Organic–inorganic metal-halide perovskites are the most sought materials for photovoltaics (PV) due to the unprecedented development on their power conversion efficiency (PCE) during the past decade, increasing from 3.8% in the first report to the recently certified 26.1% for single-junction devices.[1,2] Numerous attractive features of perovskites include their superior properties, such as their high absorption coefficient,[3–6] excellent defect tolerance,[7–9] long carrier lifetime and diffusion length,[4,10–15] ambipolar charge transport,[16–20] and low exciton binding energy.[21–23] Most highly efficient perovskite solar cells

(PSCs) were achieved using lead (Pb)-based perovskites with a typical bandgap close to 1.5 eV; note that this bandgap range is still not ideal for reaching the Shockley–Queisser (SQ) radiative limit for single-junction solar cells.[24] A unique bandgap bowing effect has been shown as an effective approach to reduce the perovskite bandgap to ≈1.2 eV by partially replacing the Pb component with tin (Sn) on the B-site of the perovskite structure.[24–26] This opens the opportunity for all-perovskite tandem solar cells—consisting of wide-bandgap (WBG) Pb perovskites as a top subcell for capturing high-energy photons and narrow-bandgap (NBG) mixed Sn-Pb perovskites as a bottom subcell for harvesting low-energy photons—that can potentially surpass the SQ radiative limit for single-junction solar cells.[12,13,26–40]

The general research on mixed Sn-Pb perovskites (including pure Sn perovskites) began in 2014. Similar to the development of Pb-based PSCs, mixed Sn-Pb- or Sn-based PSCs also adopted the regular (n-i-p) and inverted (p-i-n) device structures. In 2014, Hayase et al. first reported n-i-p structured Sn-Pb PSCs with PCEs of 4.2% by using the $MASn_{0.5}Pb_{0.5}I_3$ composition and the mesoporous titanium oxide (TiO_2) scaffold as the electron transport material (ETM). The bandgap of this composition is ≈1.17 eV, much narrower than pure Pb and pure Sn perovskites.[41,42] The p-i-n device architecture of mixed Sn-Pb PSCs was first reported by Kanatzidis et al. in 2014; in this study, a bandgap of ≈1.17 eV was obtained with 50% Sn, achieving the best PCE of 7.3%.[43] Since then, various advances have quickly pushed the PCEs of mixed Sn-Pb PSCs to more than 10%[12,36,44,45] and even exceeding 23%;[38,46,47] however, there is still significant room for improvement compared to pure Pb-based PSCs.

Benefiting from the progress of mixed Sn-Pb perovskites, their application in monolithic two-terminal (2T) tandem solar cells has also achieved unprecedented progress, leading to the recent demonstration of a certified PCE of 29.1%.[48] Recent rapid advances on all-perovskite tandems have made this PV technology attractive for industry application, similar to other perovskite-based tandems (e.g., perovskite-silicon (Si),[49–53] perovskite-copper indium gallium diselenide (CIGS),[54–56] and perovskite-organic;[57,58]) however, further improvement on the efficiency and stability of all-perovskite tandems is still limited by both WBG and NBG subcells, especially for NBG mixed Sn-Pb

F. Yang, K. Zhu
Chemistry and Nanoscience Center
National Renewable Energy Laboratory
Golden, CO 80401, USA
E-mail: kai.zhu@nrel.gov

The ORCID identification number(s) for the author(s) of this article can be found under https://doi.org/10.1002/adma.202314341

ADVANCED
SCIENCE NEWS
www.advancedsciencenews.com
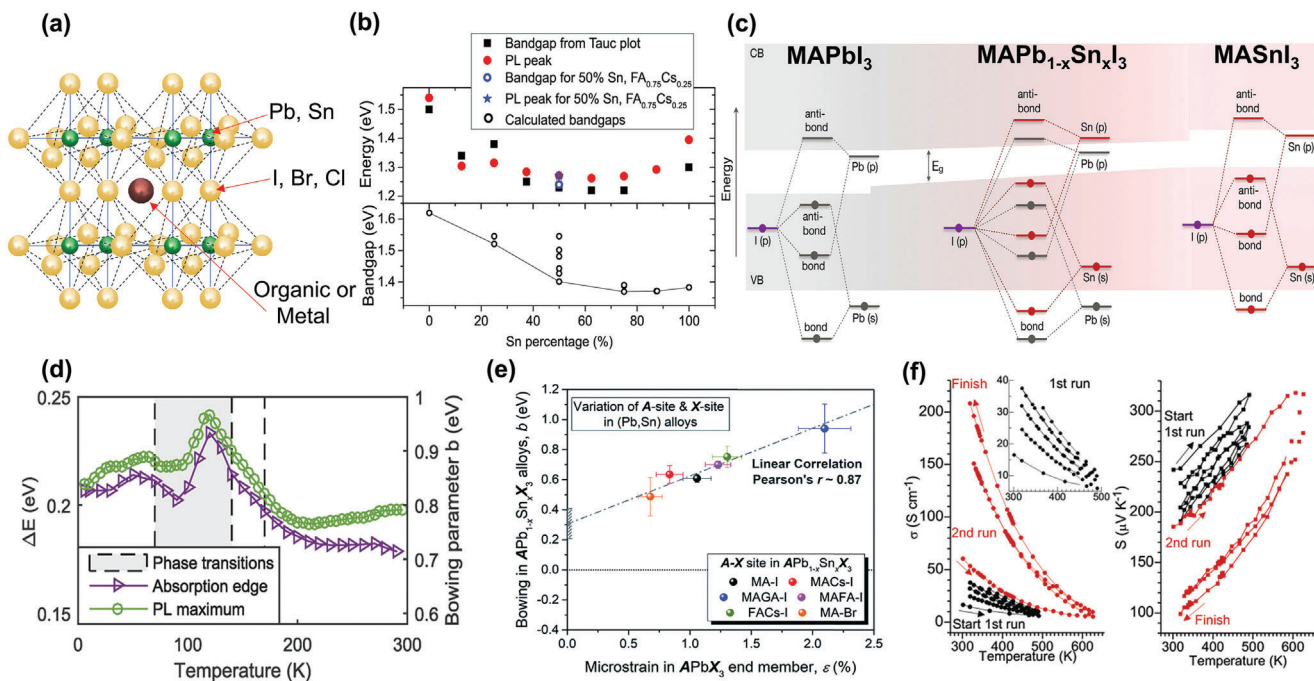
**ADVANCED
MATERIALS**
www.advmat.de

Figure 1. a) Schematic of mixed Sn-Pb perovskite crystal structure. b) Comparison of the bandgap values of Sn-Pb perovskites based on the absorption measurement (black squares) and first-principles calculations (black circles). The corresponding photoluminescence (PL) peak positions are denoted as red solid circles. Reproduced with permission.[26] Copyright 2016, AAAS. c) Schematic illustration of the origin of the bandgap bowing in $MA(Pb_{1-x}Sn_x)I_3$. The shaded regions with thick lines show the corresponding molecular orbital picture of the electronic bands. Reproduced with permission.[60] Copyright 2018, American Chemical Society. d) The bandgap bowing parameters were calculated by fitting absorption edge energy with a parabola model (purple triangles) and PL peak energy (green circles). The shaded area indicates the phase transition region and an extra phase transition of $FASnI_3$ is marked with a dashed line at 170 K. Reproduced with permission.[61] Copyright 2018, Wiley-VCH. e) Bandgap bowing plots for $APb_{1-x}Sn_xX_3$ material versus microstrains in their respective $APbX_3$ compositions. Reproduced with permission.[62] Copyright 2019, The Royal Society of Chemistry. f) Temperature-dependent electrical conductivity (left panel) and Seebeck coefficients (right panel) of a $CsSnI_3$ perovskite. Reproduced with permission.[63] Copyright 2012, American Chemical Society.

perovskites. In particular, the stability progress of all-perovskite tandems is significantly lagging behind their efficiency advances.

Here, we review the recent progress of mixed Sn-Pb perovskite for single-junction PSCs and tandem solar cells. We summarize the properties of mixed Sn-Pb perovskites and discuss the factors contributing to the instability issue. Next, we review recent advances on improving the performance of mixed Sn-Pb PSCs, focusing on various reported approaches, including additives and solvents engineering, interfacial treatment, solvent extraction control, and hole transport materials (HTMs). We also highlight the recent progress of all-perovskite tandem solar cells using Sn-Pb perovskites as the bottom cells. Finally, we provide our perspective and outlook for further development of Sn-Pb perovskites in both efficiency and stability for single-junction and tandem PV applications.

2. Structural and Optoelectronic Properties of Mixed Sn-Pb Perovskites

2.1. Anomalous Bandgap Bowing Behavior

Figure 1a shows the schematic of the mixed Sn-Pb perovskite crystal structure. It follows the general ABX_3 structure, where A is a monovalent cation such as cesium (Cs^+), formamidium (FA^+), or methylammonium (MA^+); B is a divalent metal cation

such as Sn^{2+} and Pb^{2+}; and X is halide anions such as iodide (I^-), chloride (Cl^-), and bromide (Br^-). The bandgap (E_g) of mixed Sn-Pb perovskites exhibits a unique bowing dependence on the Sn-Pb mixing ratio, as shown in Figure 1b.[25,26,43] As the Sn percentage increases from zero (pure Pb perovskite), first, the E_g decreases, reaching the minimize value, and then it increases until reaching the pure Sn perovskite. Theoretical calculations showed that the competition between the spin-orbit coupling and lattice distortion contributed to the E_g changes in $MASn_{1-x}Pb_xI_3$.[25] Snaith et al. commented that the "short-range order" of the Sn and Pb atoms is responsible for the E_g bowing effect of mixed Sn-Pb perovskites.[26] Ogomi et al. showed that the band structure of $MASnI_3$ is slightly different than that of $MAPbI_3$, where the ≈0.7-eV valance band energy downshift was only partially offset by the ≈0.2-eV conduction band energy downshift.[59] To understand this controversy, Goyal et al. calculated the electronic structure and E_g evolution with changing chemical compositions in $MA(Pb_{1-x}Sn_x)I_3$.[60] Despite the difference in calculating the absolute E_g values, all theoretical works agree on the amount of bowing (the value of b, based on the fitted curve: $E = xE_{Sn} + (1-x)E_{Pb} - x(1-x)b$), which is in agreement with experimental results. The large bowing effect is mainly attributed to the energy mismatch between Pb and Sn atomic orbitals. Figure 1c shows the atomic spin orbitals of perovskites with pure Pb, Sn, and mixed Sn-Pb compositions.[60] It is noteworthy that the band

**ADVANCED
SCIENCE NEWS**

www.advancedsciencenews.com

**ADVANCED
MATERIALS**

www.advmat.de

edges of pure MAPbI$_3$ are generally much sharper than those of pure MASnI$_3$. Because Pb-s and Pb-p atomic orbitals are stronger bonds than the corresponding Sn states, the conduction band maximum (CBM) of mixed Sn-Pb perovskite is derived from interactions between the Pb-p and I-p orbitals, whereas the valance band maximum (VBM) is derived from the Sn-s and I-p orbitals. As a result, the E_g of Sn-Pb perovskites is lower than that of either pure Pb or pure Sn perovskites.

Parrott et al. suggested that the E_g bowing behavior of mixed Sn-Pb perovskites is affected by their temperature-dependent crystal structural phase and composition, where the absorption edge was found to significantly change with temperature along with two phases of Sn containing compositions that exist in different temperature regimes (Figure 1d); this work points to the importance of controlling the structure and composition for developing Sn-Pb perovskites.[61] In 2019, Rajagopal et al. showed that incorporating Sn in Pb-based perovskite structures could mitigate the microstrains in perovskite crystals, resulting in reduced octahedral tilting and increased octahedral distortion (Figure 1e).[62] A series of perovskite compositions containing mixed Sn-Pb with varying ratios were examined, and a higher microstrain was found to correlate with a more pronounced E_g bowing effect in Sn-Pb perovskites. This study further indicated that the Sn and Pb energy level mismatch can also affect the bowing effect. Note that although the E_g bowing effect of Sn-Pb perovskites has been consistently observed by many groups, more systematic fundamental studies are still needed to understand the origins and implications of the bowing effect.

2.2. Origin of Instability of Mixed Sn-Pb Perovskites

Partially replacing Pb with Sn for mixed Sn-Pb perovskites typically suffers from instability challenges compared to pure Pb-based perovskites because of the propensity of Sn^{2+} to be easily oxidized into Sn^{4+}.[36,64] The oxidation of Sn^{2+} to Sn^{4+} in the solvent of dimethyl sulfoxide (DMSO) was observed by using nuclear magnetic resonance (NMR) spectroscopy and X-ray absorption near-edge structure (XANES) spectroscopy.[65–67] The solvent-induced oxidation problem represents a key challenge for fabricating highly efficient and stable Sn-Pb PSCs. Note that Sn-Pb perovskites have distorted crystal structures because the Sn element has a smaller atomic radius (1.02 Å) than Pb (1.19 Å); both Sn and Pb are from the same group in the periodic table, Group IVA.[44] The different outer electron structures of Sn^{2+} and Pb^{2+} lead to an easier oxidation potential for Sn^{2+} than Pb^{2+}; Sn^{2+} has a lone pair of electrons on the 5s orbital ([Kr]5s^{2}4d^{10}) compared to the 6s orbital of Pb^{2+} ([Xe]6s^{2}4f^{14}5d^{10}), resulting in a weaker shielding of the occupied 4d orbital.[68,69]

X-ray diffraction (XRD) along with thermogravimetric analysis (TGA) have also been applied to observe the oxidation of Sn^{2+} of mixed Sn-Pb perovskites.[70] The characteristic XRD peak intensity of Sn-Pb perovskites aged in dry air significantly decreases with increasing aging time and Sn ratio. Similar evidence was obtained from the TGA characterization, where a more rapid mass loss of a pure Sn perovskite at a lower temperature was observed in the air compared to the test conducted in N$_2$. Compared to pure Sn perovskites, mixing Sn and Pb was shown to change the degradation mechanism, leading to significantly improved sta-

bility than would be expected simply based on the reduced Sn fraction in the Sn-Pb perovskite. It is noteworthy that the oxidation of Sn^{2+} is usually accompanied by an orange-red color of the Sn-based precursor solution.[36,70]

The oxidation of Sn^{2+} can usually occur in multiple stages during perovskite film preparation (precursor solution, wet film coating, solid film formation). The Sn^{2+} oxidation can result in the Sn vacancy formation, causing an increased concentration of holes, which agrees with the increased electrical conductivity and the decreased Seebeck coefficient for aged Sn-Pb perovskite films (Figure 1f).[63] The increase in the p-type conductivity associated with Sn vacancy formation is often accompanied by enhanced non-radiative recombination, which, in turn, can lead to a significant open-circuit voltage (V_{OC}) loss in PSCs.[15] Because of instable Sn^{2+}, more defect states can be generated in Sn-Pb perovskites than in pure-Pb perovskites, which further exacerbates the instability issue for Sn-Pb PSCs.[71] Note that substantial trap states can be generated even at ≈1% of Sn in FA$_{0.83}$Cs$_{0.17}$Pb$_{1-x}$Sn$_x$I$_3$.[72] Interestingly, the optoelectronic properties of mixed Sn-Pb perovskites are often restored when the Sn ratio is increased to 30–60% compared to the "defective" 0.5–20% range; as a result, the best-performing mixed Sn-Pb PSCs generally have Sn within the 30–60% range.

Another key factor for defect formation in Sn-Pb perovskites is the fast crystallization associated with high Lewis acidity of Sn^{2+} and fast coordination between Sn^{2+} and the organic component.[73] The fast crystallization usually generates small grains with a high density of grain boundaries, where recombination/trap centers can easily form.[74,75] The residual strain of mixed Sn-Pb perovskite films caused by the contraction of grains due to Sn alloying was also shown to cause defect formation and poor carrier extractions.[76,77] The weaker bonding strength of Sn-I than Pb-I would cause a depletion of organic cations at the perovskite film surface for additional trap formation.[78] The defect states can enhance the chemical degradation and facilitate ion migration, contributing to instability and hysteresis issues.[15,79]

Moreover, the interfaces of contact layers also induce the instability of Sn-based PSCs. The charged carriers can accumulate at interfaces of the electron or hole transport layer (ETL or HTL) if the energy level of perovskite is misaligned with the ETL or HTL.[80] Ineffective charge collection/separation at the ETL/HTL interfaces can also enhance nonradiative charge recombination near the interface regions, leading to instability and hysteresis of PSCs.[81–83]

3. Progresses on Performance and Stability of Mixed Sn-Pb NBG Perovskites

With extensive research during the past several years, single-junction Sn-Pb PSCs have made significant advances, with a PCE exceeding 23%;[38,46,47] the corresponding PV status of Sn-Pb PSCs is summarized in **Figure 2** and Table S1, Supporting Information. The operational stability status of Sn-Pb single-junction devices is summarized in Table S2, Supporting Information. All-perovskite tandem solar cells have also progressed to reach a certified PCE of 29.1%.[48] The field has largely focused on Sn-Pb perovskites with E_g of ≈1.25 eV, which is suitable as the bottom cell in a tandem. At present, for single-junction Sn-Pb PSCs, the V_{OCc} and fill factor (FF) are close to or slightly more than 90% of
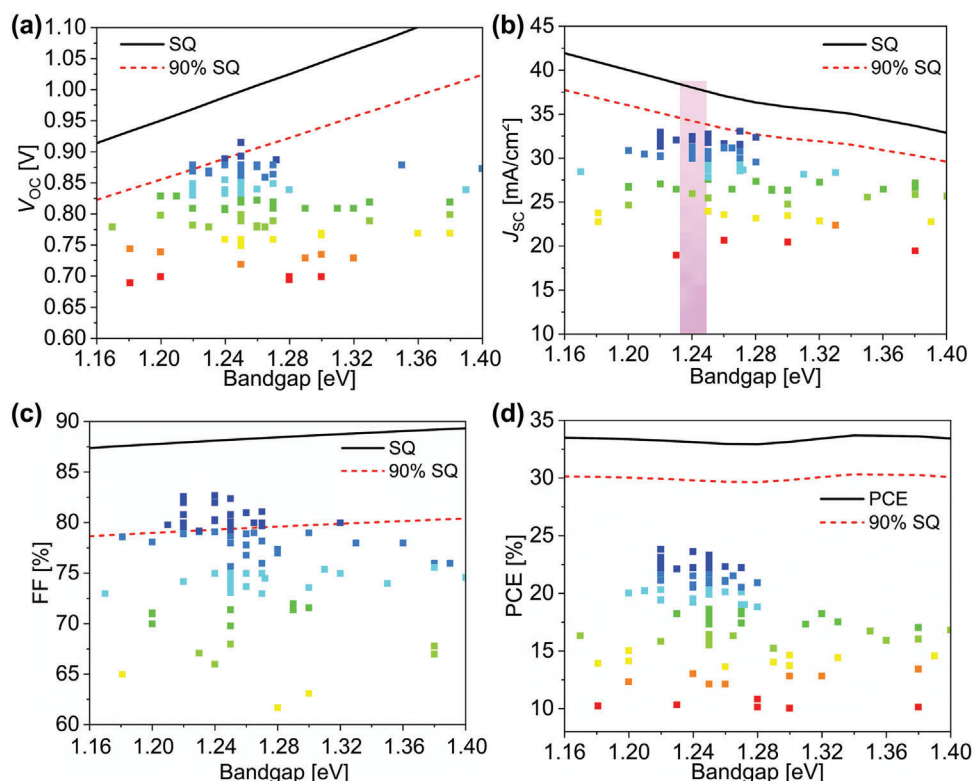
**ADVANCED
SCIENCE NEWS**

www.advancedsciencenews.com

**ADVANCED
MATERIALS**

www.advmat.de

Figure 2. PV status summary of mixed Sn-Pb PSCs with bandgap from 1.16 to 1.4 eV: a) V_{OC}; b) J_{SC}; c) FF; and d) PCE. SQ: Shockley–Queisser. The black solid line denotes the SQ radiative limit. The red dotted line denotes 90% of the SQ limit.

the SQ radiative limit. Increasing the short-circuit current density (J_{SC}) of mixed Sn-Pb PSCs has become a key challenge due to the film thickness limitation and relatively weak absorption near the absorption edge region. Another critical challenge of Sn-Pb PSCs is their poor operational stability, especially at elevated temperatures (e.g., >50 °C). These challenges are usually associated with the Sn^{2+}-to-Sn^{4+} oxidation issue, which further leads to increased background hole carrier density, shorter charge carrier diffusion length, higher recombination loss, and a lower V_{OC} and FF in a device. Numerous efforts have been explored to improve the performance and stability of Sn-Pb PSCs. In this section, we review recent progress on improving Sn-Pb perovskite films and solar cells. We highlight a wide range of strategies, including perovskite precursor additives, solvent tuning, interfacial engineering, solvent extraction control, and HTL engineering.

3.1. Additive Engineering

3.1.1. Halide Ion Salt Additives

The application of additives is one of the most useful and common approaches to improve the optoelectronic properties of perovskite thin films for high-performance solar cells. Tin fluoride (SnF_2) is frequently used as a halide salt additive for Sn-based perovskites to suppress the Sn^{2+}-to-Sn^{4+} oxidation due to the strong reducibility for suppressing the hole carrier density in Sn-based perovskite films.[84–90] Typically, 20–30 mol% of SnF_2 relative to SnI_2 is used in a Sn-Pb perovskite precursor composition to improve the current density with reduced hysteresis.[91,92] Because the radius of F^- is much smaller than I^-, the F^- of SnF_2 cannot be incorporated in the perovskite crystal structure; therefore, most SnF_2 is accumulated at the surface of the perovskite grains, which is supported by time-of-flight secondary-ion mass spectrometry (ToF-SIMS) measurements (**Figure 3**a).[15,46] To solve this issue, Kapil et al. reported on the use of precoordinated SnF_2-DMSO to reduce trap densities and improve charge transport abilities for better device efficiency.[93] In another study, Ripolles et al. reported that the use of the precoordinated complex $[SnF_2(DMSO)]_2$ can reduce the trap states and improve transport recombination at the interface compared to SnF_2 salt.[94] In this study, the use of $[SnF_2(DMSO)]_2$ reduced the E_g of Sn-Pb perovskite film, shifted the lowest unoccupied molecular orbital (LOMO) for better electron carrier extraction (Figure 3b), and reduced the Urbach energy (E_u) from 49 meV using SnF_2 to 20 meV using $[SnF_2(DMSO)]_2$.

Pre-synthesized complexes of SnX_2 (X: F^- or Cl^-) with FACl were shown to enhance the utilization of SnX_2 and improve the structural/optoelectronic/mechanical properties of Sn-Pb perovskite thin films. Zong et al. showed that the use of the SnF_2-3FACl complex can improve the solubility of SnF_2, and SnF_2 was found to be uniformly distributed at grain boundaries and FACl enlarged the perovskite grains during annealing.[95] The accumulated SnF_2 at grain boundaries helps suppress the ingress of moisture and oxygen, leading to enhanced moisture, thermal, and light stability of the perovskite film. The improved stability
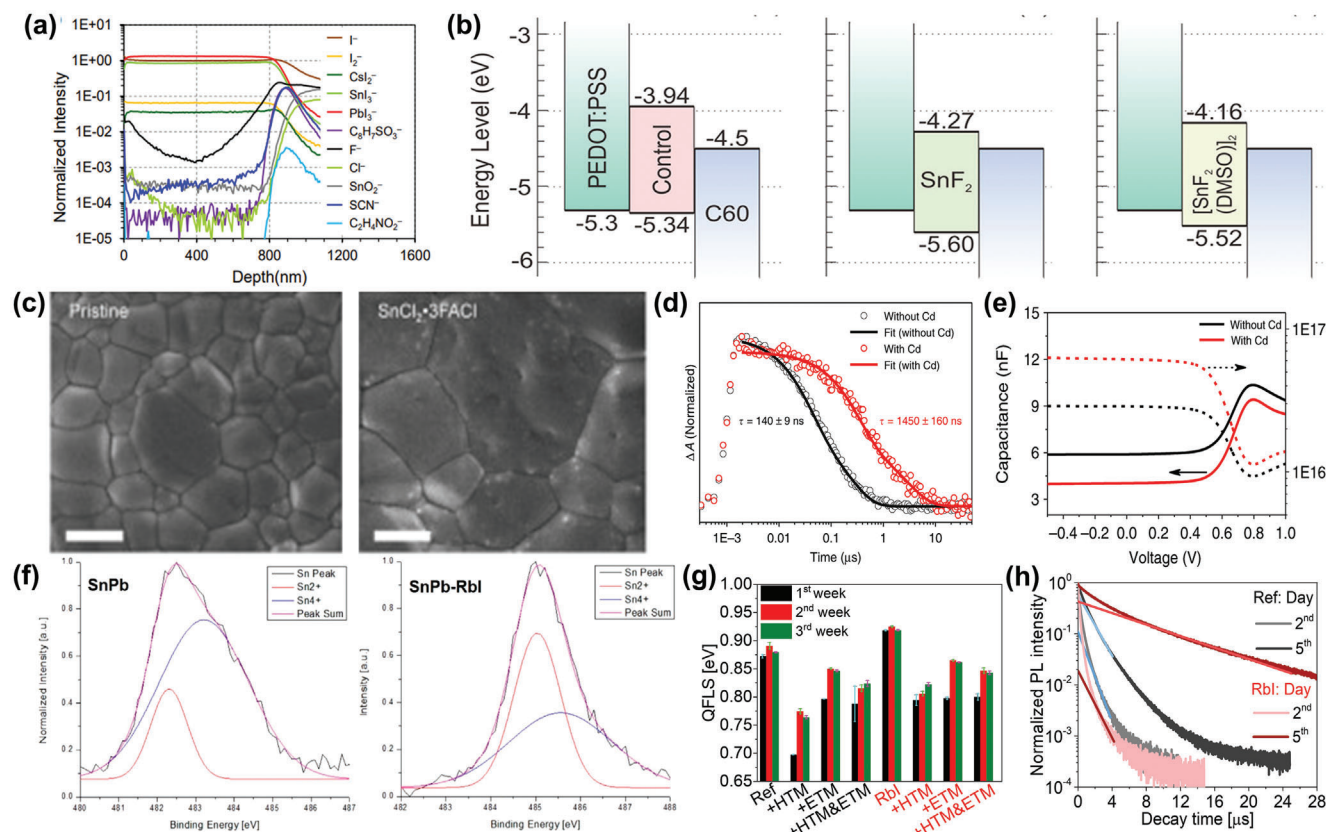
ADVANCED
SCIENCE NEWS
www.advancedsciencenews.com

ADVANCED
MATERIALS
www.advmat.de

Figure 3. a) ToF-SIMS depth profiles of Sn-Pb perovskite films fabricated on a PEDOT:PSS/FTO substrate. Reproduced with permission.[46] Copyright 2022, The Royal Society of Chemistry. b) Energy level diagram of control perovskite (left), perovskites with SnF_2 (middle), and perovskite with $[SnF_2(DMSO)]_2$ complex (right). Reproduced with permission.[94] Copyright 2018, American Chemical Society. c) Top view of scanning electron microscopy (SEM) images of perovskite films without (left) and with (right) $SnCl_2\cdot3FACl$ additive, respectively (scale bar: 500 nm). Reproduced with permission.[96] Copyright 2021, Elsevier. d) Transient absorption of perovskite films with and without Cd^{2+} ions and e) capacitance–voltage curves of PSCs with and without Cd^{2+} ions at 295 K. Reproduced with permission.[12] Copyright 2020, Nature Springer. f) XPS analysis of the oxidation state of the Sn $3d_{5/2}$ peak of Sn-Pb perovskite films with and without KI and RbI additives. Reproduced with permission.[98] Copyright 2022, American Chemical Society. g) QFLS values of perovskites with ETMs and/or HTMs measured on the first, second, and third week of storage in an N_2-filled glove box and h) TRPL comparison of perovskites on the second and fifth day of storage in an N_2-filled glove box. Reproduced with permission.[15] Copyright 2023, Wiley-VCH. Ref: control perovskite; RbI: perovskite with RbI additive; ETM: C_{60}; HTM: PEDOT:PSS on ITO.

was attributed to the continuous grain-boundary passivation with SnF_2-3FACl, increased grain size, and improved Sn^{2+}-rich grain boundary region. As a result, the PSC sustained 90% of its initial performance after storage in the ambient condition compared to the control sample (76.7%). In a separate study, the $SnCl_2$-3FACl additive was shown to not only increase the apparent size of Sn-Pb perovskite grains but also reduce the residual stresses of the perovskite film (Figure 3c).[96] In this study, the use of $SnCl_2$-3FACl was also shown to reduce the dark current density by two orders of magnitude in devices, which indicates a significantly reduced defect density. With the improvement in the microstructure and the reduction in the defect density, the efficiency of Sn-Pb PSCs increased to 19% and sustained more than 80% of the initial performance after 750-h maximum power point (MPP) tracking at 45 °C.

Other types of metal halides (e.g., ZnI_2, CdI_2, RbI) have also shown promise for improving Sn-Pb perovskite quality. ZnI_2 was incorporated in Sn-Pb perovskites, generating a uniform distribution of Sn^{2+} in the perovskite film, leading to enhanced air stability because of the reduced Sn-rich cluster and photolumi-

nescence lifetime exceeding 1 μs.[97] Using a small amount (0.03 mol%) of CdI_2 additive was also shown to increase the carrier lifetime and reduce the background p-type conductivity in Sn-Pb perovskite thin films.[12] The use of the CdI_2 suppresses atomic vacancies and increases the carrier diffusion length up to 2.72 μm compared to 0.49 μm for the reference sample (Figure 3d), allowing for the use of thick (>1-μm) perovskite films to gain higher light trapping. Temperature-dependent thermal admittance spectroscopy measurements showed that the use of CdI_2 also reduced the trap density in a device by more than one order of magnitude (Figure 3e).

Hayase et al. reported on the use of RbI as an A-site additive in an Sn-Pb perovskite precursor to improve the perovskite crystallinity and film morphology and to facilitate charge transfer associated with a better interfacial energy alignment.[98] X-ray photoelectron spectroscopy (XPS) measurements suggest that the use of the RbI additive suppressed the amount of Sn^{4+} (Figure 3f), reducing the carrier concentration from 5.75×10^{15} to 1.66×10^{15} cm^{-3} and increasing the carrier mobility from 14.0 to 22.5 cm^2 V^{-1}. By using 2 mol% RbI, the Sn-Pb PSCs achieved

ADVANCED
SCIENCE NEWS

www.advancedsciencenews.com

**ADVANCED
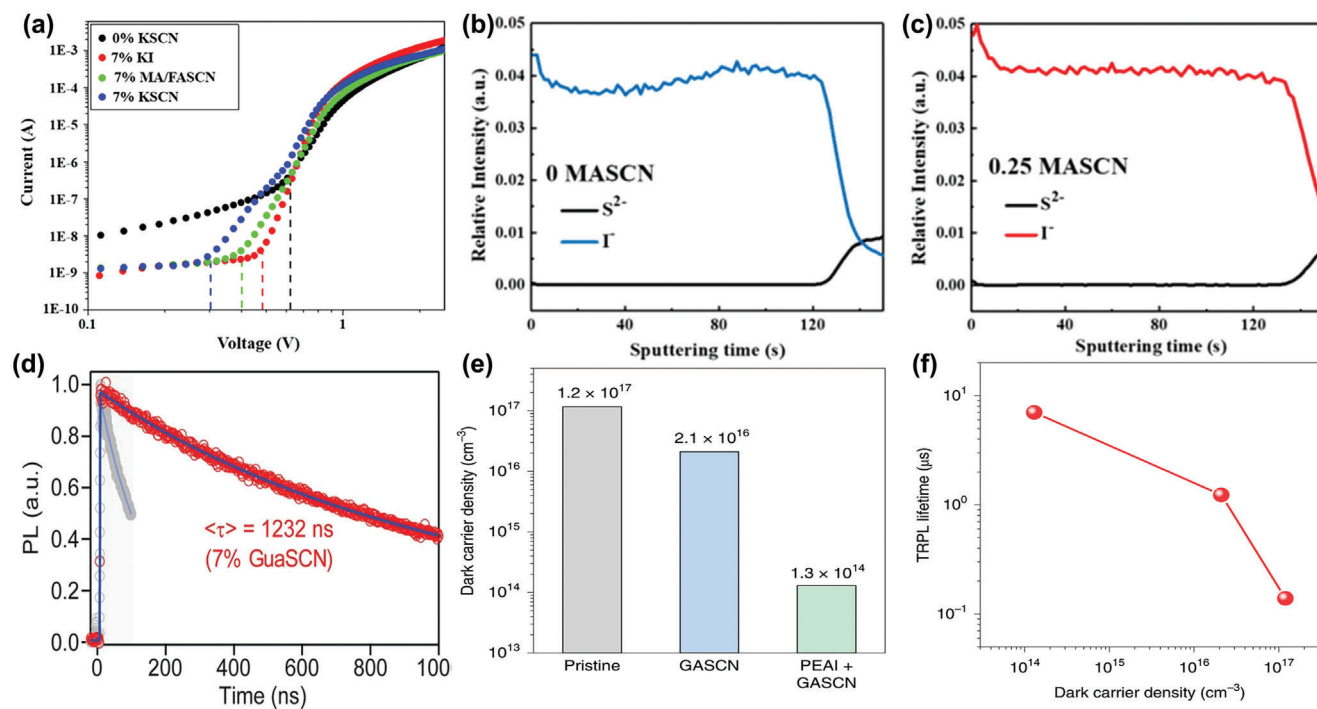MATERIALS**

www.advmat.de

Figure 4. a) Dark J–V curves of Sn-Pb PSCs with and without the KSCN additive. Reproduced with permission.[100] Copyright 2020, Wiley-VCH. Comparison of ToF-SIMS depth profiles of the S^{2-} and I^{-} as a function of the sputtering time for perovskite b) without and c) with 0.25% MASCN. Reproduced with permission.[101] Copyright 2018, Wiley-VCH. d) TRPL comparison of the Sn-Pb perovskite films without (gray) and with 7% GuaSCN (red). Reproduced with permission.[13] Copyright 2020, AAAS. e) Hall measurement of the dark carrier density and f) their impact on the TRPL lifetime of Sn-Pb perovskite films without and with additives as indicated. Reproduced with permission.[14] Copyright 2022, Nature Springer.

>21% efficiency. Yang et al. also reported on the use of RbI in MA-free Sn-Pb perovskites.[15] In this study, RbI was found to increase the quasi-Femi-level-splitting (QFLS) value to 0.925 eV in a film and 0.847 eV in a device compared to 0.89 and 0.815 eV of a reference film and device, respectively (Figure 3g), indicating significantly reduced recombination losses. The carrier lifetime was also increased to more than 9 µs with the RbI additive according to transient photoluminescence (TRPL) measurements (Figure 3h). As a result, the device showed >20% PCE compared to the reference device, with an average V_{OC} improvement of ≈61 mV. These two studies using the RbI additive also evidenced the improved stability of Sn-Pb perovskite films and cells; the improved stability is associated with the passivated trap states, lowered background hole doping, and reduced recombination losses of perovskite films and interfaces.

3.1.2. SCN⁻ Salt Additives

Thiocyanate (SCN⁻) salts are often used as additives to improve the performance of Sn-Pb PSCs; typical SCN⁻ salts include $Pb(SCN)_2$,[34,72,99] KSCN,[99,100] MASCN,[101] GuaSCN,[13,14] and NH_4SCN.[46] Snaith and coworkers used an additional 6 mol% of $Pb(SCN)_2$ to investigate the optoelectronic properties and PV characteristics of $((HC(NH_2)_2)_{0.83}Cs_{0.17})(Pb_{1-y}Sn_y)I_3$ perovskites and found a "defectiveness" zone of Sn-Pb perovskites comprising ≈0.5–20% Sn.[71] In another study, KSCN was used as an additive in $FA_{0.5}MA_{0.5}Pb_{0.5}Sn_{0.5}I_3$ perovskites and was shown to in-

crease the apparent grain size with enhanced crystallization.[100] As a result of the KSCN treatment, the bulk defects were significantly reduced based on the space-charge-limited current measurement (**Figure 4**a). Lian et al. reported the use of MASCN as a multifunctionality additive for $FAPb_{0.7}Sn_{0.3}I_3$ PSCs.[101] They found a strong coordinated function between SCN⁻ and metal ions (Pb^{2+} and Sn^{2+}) in perovskites. It is interesting that the Sn-Pb perovskite precursor maintained a light yellow state after 30 min in ambient conditions and was still functional after 124 days of storage in an N_2 glove box because of the reduced oxidation of Sn^{2+} ions with the use of MASCN additive. In addition, the SCN⁻ was found to be volatile during annealing, which improved the permeation of MAI in a two-step approach through the pores and cracks from SCN⁻ volatilization (Figure 4b,c).

Tong et al. employed GuaSCN as an additive to improve $(FASnI_3)_{0.6}(MAPbI_3)_{0.4}$ perovskites with reduced defect states at the grain boundaries and film surfaces as well as increased carrier diffusion length to ≈2.5 µm (Figure 4d).[13] The improvement was attributed to the formation of 2D barrier structures suppressing oxygen penetration. As a result, the efficiency of Sn-Pb PSCs increased to more than 20% for the first time. By adding PEAI to GuaSCN as additives in the $(FASnI_3)_{0.6}(MAPbI_3)_{0.4}$ perovskite precursor, the authors further demonstrated the formation of a quasi-2D structure, $(PEA)_2GAPb_2I_7$, at the grain boundaries, pushing the Sn-Pb perovskite to reach a dark carrier density as low as ≈1.3×10^{14} cm^{-3} (Figure 4e) and a carrier lifetime up to ≈9.2 µs (Figure 4f)).[14] As a result, the best V_{OC} of Sn-Pb PSCs increased to 0.916 V with a 22.1% PCE, which was
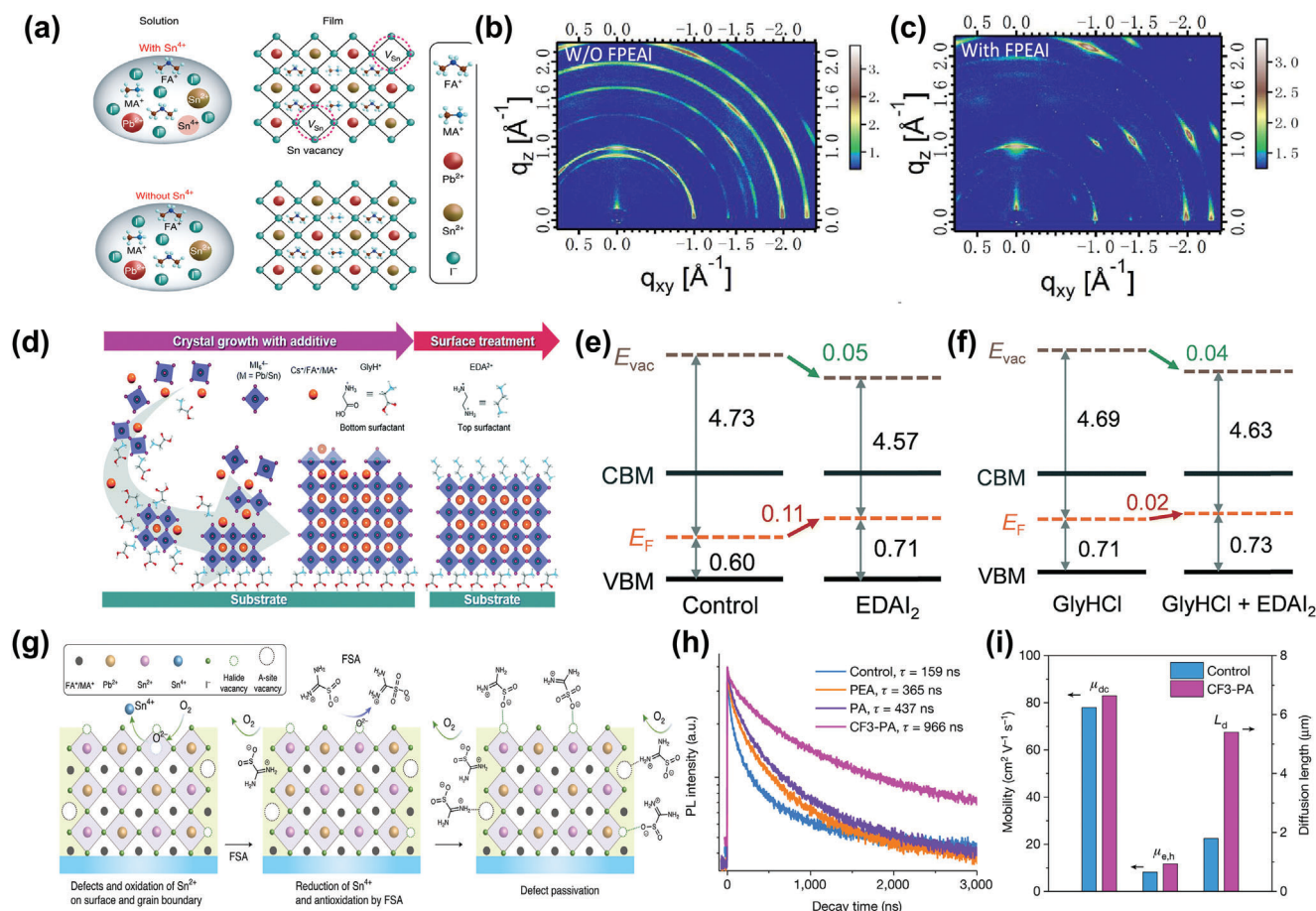
**ADVANCED
SCIENCE NEWS**

www.advancedsciencenews.com

**ADVANCED
MATERIALS**

www.advmat.de

Figure 5. a) Schematic illustration of Sn^{4+} induced formation of Sn vacancies and their reduction based on Sn powder suppression in Sn-Pb perovskites. Reproduced with permission.[36] Copyright 2019, Nature Springer. GIWAXS patterns of Sn-Pb perovskites b) without and c) with 3.75% FPEAI additive. Reproduced with permission.[102] Copyright 2020, American Chemical Society. d) Schematic illustration of the interfacial modification of Sn-Pb perovskites by using the GlyHCl additive and surface-treated agent EDAI$_2$, e) along with the energetic diagrams of perovskite with EDAI$_2$ and f) perovskite with GlyHCl or EDAI$_2$+GlyHCl. Reproduced with permission.[46] Copyright 2020, the Royal Society of Chemistry. g) Schematic illustration of FSA-induced passivation in Sn-Pb perovskites. Reproduced with permission.[37] Copyright 2020, Nature Springer. h) TRPL spectra and i) diffusion length of perovskite with additives as indicated. Reproduced with permission.[32] Copyright 2022, Nature Springer.

the highest V_{OC} achieved for mixed Sn-Pb PSCs with a similar bandgap. The small V_{OC} deficit (0.916 V for the target device versus 0.85 V for the control device) is enabled by the elongated TRPL lifetime, reduced trap states and recombination losses, and decreased background carrier doping (much lower dark current density). In addition, the PSCs maintained 82% PCEs after 1830-h tracking in N$_2$. These two studies indicated that high-quality Sn-Pb perovskite films could enable good operational stability of Sn-Pb PSCs. In addition, the 2D materials at the perovskite film surface could block oxygen penetration for abetter stability of the corresponding solar cells.

3.1.3. Other Additives

To suppress the Sn^{2+} oxidation for Sn-Pb perovskites, Tan et al. introduced metallic Sn powder in the perovskite precursor; the mechanism is illustrated in **Figure 5a**.[36] They found that the carrier lifetime improved from 3 to 43 ns and the diffusion length

increased from 0.75 to 2.99 μm by using Sn powder. Meanwhile, the hole concentration of Sn-Pb perovskites decreased from 1.4×10^{16} to 0.54×10^{16} cm^{-3} with the Sn powder additive. As a result, the Sn-Pb PSCs using Sn powder in the precursor achieved greater than 21% PCE with 0.84-V V_{OC} compared to 18.3% PCE with 0.811-V V_{OC} for the control sample.

A 2D capping layer based on organic additives represents another effective approach to protect Sn-Pb perovskites from oxidation; examples include the use of 2-(4-fluorophenyl) ethylammonium iodide (FPEAI)[102] and 3-(aminomethyl) piperidinium (3AMP^{2+}).[103] When adding FPEAI to (MAPbI$_3$)$_{0.75}$(FASnI$_3$)$_{0.25}$ perovskites, the grazing incidence wide-angle x-ray scattering (GIWAXS) demonstrated sharp and discrete Bragg spots (Figure 5b,c) along with a few extra peaks (574, 631, and 656 nm) in the photoluminescence spectra; these features correspond to the 2D perovskite with n values of 2, 3, and 4.[102] Moreover, FPEAI treatment promotes the vertical alignment of highly oriented 3D Sn-Pb perovskite crystals mixed with quasi-2D structures, leading to improved vertical carrier extraction and

**ADVANCED
SCIENCE NEWS**

www.advancedsciencenews.com

**ADVANCED
MATERIALS**

www.advmat.de

transportation. In another study using 3AMP^{2+}, the two nitrogen groups of 3AMP^{2+} are shown to form a 2D Dion-Jacobson/3D phase, (3AMP)(FA$_{0.5}$MA$_{0.5}$)$_3$(Pb$_{0.5}$Sn$_{0.5}$)$_4$I$_{13}$, that functions as an additive for reducing the defect states and increasing the carrier lifetime in Sn-Pb perovskites, leading to increased V_{oc} up to 0.87 V and a champion PCE of 20.09%.[103] The encapsulated mixed Sn-Pb PSCs kept better continuous operational stability under illumination in ambient air with 20%−50% humidity for over 100 h due to the 2D perovskite capping layer.

Some additives can affect the interfaces between perovskites and the charge transport layer. For example, the interface of an Sn-Pb perovskite/PEDOT:PSS can be affected by the additive of glycine hydrochloride (GlyHCl) in the perovskite precursor;[104] the MA head of GlyH$^+$ can bind to the perovskite surface and stabilize the formation of larger particles as nucleation centers for perovskite film growth.[105] As the Gly group chain increases (n = 4, 6, and 8), Gly-based, low-dimensional, Ruddlesden–Popper perovskites were found on top of 3D perovskites with increasing perovskite grain size. Wakamiya et al. introduced GlyHCl in the Sn-Pb perovskite precursor to improve perovskite crystallinity, and with additional surface treatment using ethylenediammonium diiodide (EDAI$_2$), the carrier lifetime increased to 4.9 µs.[46] Figure 5d schematically shows that GlyHCl and EDAI$_2$ are, respectively, accumulated at the perovskite/HTL and perovskite/ETL interfaces, which is supported by ToF-SIMS measurements. These treatments also modified the interfacial energy alignment for improved carrier extraction (Figure 5e,f). As a result, the device showed an improved V_{OC} from 0.79 to 0.89 V and a champion PCE of 23.6%. The unencapsulated mixed Sn-Pb PSCs sustained >80% of initial efficiency after 200-h continuous illumination in N$_2$ environment, which can be attributed to the reduced trap states and less recombination losses.

Acid represents another group of additives that are effective for suppressing Sn^{2+} oxidation in Sn-Pb perovskites, such as ascorbic acid[106] and formamidine sulfinic acid (FSA).[37] Ascorbic acid has a better antioxidative function than SnF$_2$ for reducing Sn vacancies, as reflected from the stable absorbance (light yellow precursor) and increased carrier lifetime.[106] Tan et al. reported the use of FSA, a surface anchoring zwitterionic antioxidant, as an additive for FA$_{0.7}$MA$_{0.3}$Pb$_{0.5}$Sn$_{0.5}$I$_3$ (Figure 5g).[37] In this study, FSA was found to suppress Sn^{2+} oxidation, as evidenced by comparing the precursor color and absorptance spectra in air; it also improved the reproducibility and homogeneity of perovskite from photoluminescent mapping images. As a result, the PCE of single-junction Sn-Pb PSCs increased to 21.7%. They also obtained a certified 24.2% PCE for 1-cm^2 all-perovskite tandem devices for the first time; the FSA-treated PSCs maintained 88% of their initial performance after more than 500-h MPP tracking. To improve the short-circuit current density (J_{SC}) of all-perovskite tandem solar cells, the thickness of Sn-Pb perovskites is a critical factor for achieving high J_{SC} and PCE of solar cells. Lin et al. introduced 4-trifluoromethyl-phenylammonium (CF3-PA) as an additive for Sn-Pb perovskites,[32] which exhibited a stronger perovskite surface passivator interaction than phenethylammonium. With the addition of CF3-PA, the Sn-Pb perovskite showed fewer Sn^{4+} vacancies, longer carrier lifetime (Figure 5h) and diffusion length (>5 µm), and higher mobility of the limiting carrier (up to 11.7 cm^2 V^{-1}s^{-1}) (Figure 5i). Consequently, the Sn-Pb PSCs increased the PCE to 22.2% with a J_{SC} of 33.0 mA cm^{-2} on

a 1.2-µm Sn-Pb perovskite film, which improved the tandem J_{SC} to 16.5 mA cm^{-2} with a PCE of 26.6%. An encapsulated tandem cell also sustained 90% of its initial efficiency after 600-h MPP in ambient.

Recently, Ke et al. reported the use of aspartate hydrochloride (AspCl), a multifunctional additive, to improve Sn-Pb PSC performance. This chemical has three functional groups: Cl$^-$ can reduce iodine vacancies; the amino group can coordinate with I$^-$, suppressing trap density and mitigating I$^-$ migration; and the carboxyl group can coordinate with Pb^{2+} or Sn^{2+} to enhance perovskite integrity. Thus, this chemical showed improvement in three areas when mixed into either PEDOT:PSS HTL or perovskite ink, or used as a perovskite surface treatment agent. As a result, the V_{oc} of mixed Sn-Pb PSC reached 0.89 V compared to reference (0.81 V).[107] Yan et al. demonstrated the use of tin(II) oxalate (SnC$_2$O$_4$), with the strong reducing capability from C$_2$O$_4$$^{2-}$, to effectively suppress the Sn^{2+} oxidation and formation of Sn vacancy, leading to substantial reduction of background hole carrier doping with improved carrier lifetime. This additive also avoids the issue associated with using F$^-$ (from SnF$_2$) that aggregates at the interface limiting charge transport. By using SnC$_2$O$_4$ additive, the V_{oc} of Sn-Pb PSCs enhanced from 0.849 to 0.888 V with efficiency of 23.36%. Furthermore, the unencapsulated SnC$_2$O$_4$-based device sustained 80% of its initial performance after 1200 h thermal stress at 85 °C compared to 52% of controlled device after 600 h in N$_2$-filled glovebox.[108]

3.2. Solvent Engineering

Sn^{2+} can easily oxidize to Sn^{4+} during film preparation, resulting in a significant performance loss. However, Sn^{2+} oxidation can also occur at the precursor stage. Sargent et al. showed this oxidation pathway by using XANES measurement, where distinct peaks corresponding to Sn^{4+} were tracked using the Sn L-edge with a reduction of the S K-edge of DMSO (**Figure 6a**).[66] The conventional DMSO solvent can oxidize Sn^{2+} when the temperature exceeds 100 °C. Abate et al. also observed the evidence of Sn^{2+} oxidation when they used NMR spectroscopy to investigate the origin of Sn^{4+} of Sn-based perovskite in the solid state and solutions.[65] They found that DMSO oxidized Sn^{2+} in an acidic condition during film annealing, and they hypothesized that the redox reaction between DMSO and Sn^{2+} to form an iododimethylsulfonium iodide intermediate is catalyzed by hydroiodic acid. This reaction could be weakened at a lower temperature and in less acidic conditions. As an illustration, they showed a new, DMSO-free, solvent system to fabricate an Sn-based perovskite.[109] In this study, the solvent is based on a mixture of N,N-dimethylformamide (DMF) and 1,3-dimethyl-2-imidazolidinone (DMI) along with the addition of 4-(tert-butyl) pyridine (tBP). The use of tBP, instead of DMSO, was shown to form a strong complex with SnI$_2$ to slow down the crystallization kinetics, leading to improved film morphology and reduced defect density.

In another recent study, Zhang et al. introduced N,N′-dimethylpropyleneurea (DMPU) in the Cs$_{0.25}$FA$_{0.75}$Pb$_{0.5}$Sn$_{0.5}$I$_3$ perovskite and revealed a significant reduction of PbI$_4$$^{2-}$ and SnI$_4$$^{2-}$ in the DMF/DMPU precursor solution by using Benesi–Hildebrand analyses.[67] DMPU has a strong coordination ability

**ADVANCED
SCIENCE NEWS**

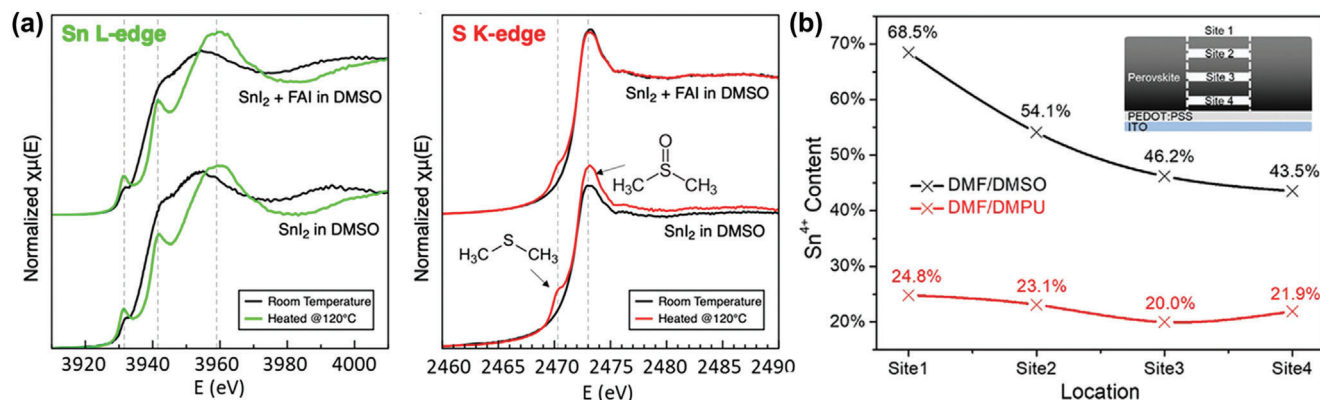www.advancedsciencenews.com

**ADVANCED
MATERIALS**

www.advmat.de

Figure 6. a) XANES characterization of Sn-based perovskite solutions before and after thermal treatment. Reproduced with permission.[66] Copyright 2020, American Chemical Society. b) Effect of DMSO and DMPU solvents on the Sn^{4+} content (based on XPS analysis of $Sn_{3d5/2}$) at different depths across the film thickness (as indicated) of Sn-Pb perovskite films. Reproduced with permission.[67] Copyright 2023, Wiley-VCH.

to form complexation with organic (FAI) and inorganic (PbI_2 and SnI_2) components, according to the Hansen solubility parameters as well as Gutmann's donor number. With this approach, they realized pure intermediate complexes, retarded crystallization, and increased grain size with better crystallinity. The oxidation of Sn^{2+} of Sn-Pb perovskites was reduced by ≈75%, and the device V_{OC} increased from 0.81 V (DMSO) to 0.88 V (DMPU) with a PCE of 22.41% for MA-free Sn-Pb PSCs. They demonstrated that the Femi level of the DMPU sample shifts up (thus more n-type) compared to the DMSO sample, with fewer defect states at the film surface and grain boundaries. To verify the DMPU impact, the Sn^{4+} signal was tracked by XPS across the film thickness, and Sn^{4+} was found to be reduced by nearly 75% (Figure 6b). With the suppression of Sn^{2+} oxidation, the stability of Sn-Pb PSCs has significantly improved compared to the typical solvent approach based on DMSO-DMF mixture. The improvement is seen under various conditions, including the humid air (30% RH), thermal stress (85 °C), or light soaking (1 sun). It is noteworthy that the device exhibited <5% degradation after aging at 85°C for 500 h. This improved thermal stability was attributed to the better thermal stability associated with DMPU in comparison to other solvents (e.g., DMSO). Thus, the chemical interaction and thermal stability should be the key factors of consideration to select new solvents to replace the typical DMSO for developing Sn-Pb PSCs.

3.3. Interfacial Engineering

The interfaces of perovskite in a device are usually prone to forming defects that can lead to degradation during device operation. The interface-related degradation is important for Sn-Pb perovskites, because the nonradiative recombination losses, Sn^{2+} oxidation, and degradation usually occur first from the interface regions; thus, interface treatment represents another key approach to improving the overall efficiency and stability of Sn-Pb PSCs.

Jayawardena et al. introduced guanidinium bromide (GABr) to treat $Cs_{0.05}FA_{0.79}MA_{0.16}Pb_{0.5}Sn_{0.5}I_3$ film to reduce recombination losses and improve the performance of solar cells (**Figure 7a**).[110] As a result of this treatment, the Fermi level increased with down-

shifted CBM and VBM and reduced the interfacial electron/hole transfer energy barrier. In another study, PEABr surface treatment was used to induce a thin layer of a 2D Ruddlesden–Popper perovskite on top of $(FASnI_3)_{0.25}(MAPbI_3)_{0.75}$, which significantly reduced the charge recombination and improved the V_{OC} by ≈70 mV.[111] An in-film (or in situ) PEAI treatment approach was reported by mixing PEAI in the ethyl acetate antisolvent when processing $Cs_{0.1}MA_{0.2}FA_{0.7}Pb_{0.5}Sn_{0.5}I_3$ perovskite film (Figure 7b).[112] Compared to the conventional PEAI posttreatment, the in situ approach formed an intermediate phase, allowing for a deeper PEA^+ penetration and passivation of the bulk of the perovskite film, leading to increased moisture resistance for better stability of the perovskite films and devices, reduced iodide residue, and suppressed recombination. The potential difference between a grain boundary and its adjacent grain interior was also reduced after the passivation treatment.

To improve the surface property of Sn-Pb perovskite films, Wakamiya et al. introduced piperazine for surface treatment to modify the surface structure and tune the interfacial energy alignment to improve charge extraction (Figure 7c).[113] A surface dipole formed with the application of the diamine, which caused the shift of the vacuum level and VBM values of perovskite films, creating a barrier for blocking holes and reducing the interfacial charge recombination. The electric field associated with the surface dipole also improved electron extraction. To further improve the performance of Sn-Pb PSCs, they introduced C_{60} pyrrolidine tris-acid (CPTA) along with piperazine to treat the perovskite film surface, which improved the TRPL lifetime and reduced recombination losses, leading to the Sn-Pb PSCs achieved 22.31% PCEs with 0.88-V V_{OC}. Note that CPTA-treated devices improved the shelf-stability to 96% of the initial efficiency compared to controlled samples (69%) after >2000 h without any encapsulations. The improved stability of mixed Sn-Pb PSCs can be ascribed to the suppressed Sn^{2+} oxidation for CPTA-treated perovskite film based on XPS analysis (Figure 7d).

Tan et al. employed a novel strategy of 3D/3D bilayer perovskite heterojunction was employed at the Sn-Pb perovskite/ETL interface.[38] The bilayer heterojunction was formed by a hybrid evaporation/solution process involving a thermal evaporating lead-halide WBG perovskite atop the Sn-Pb perovskite
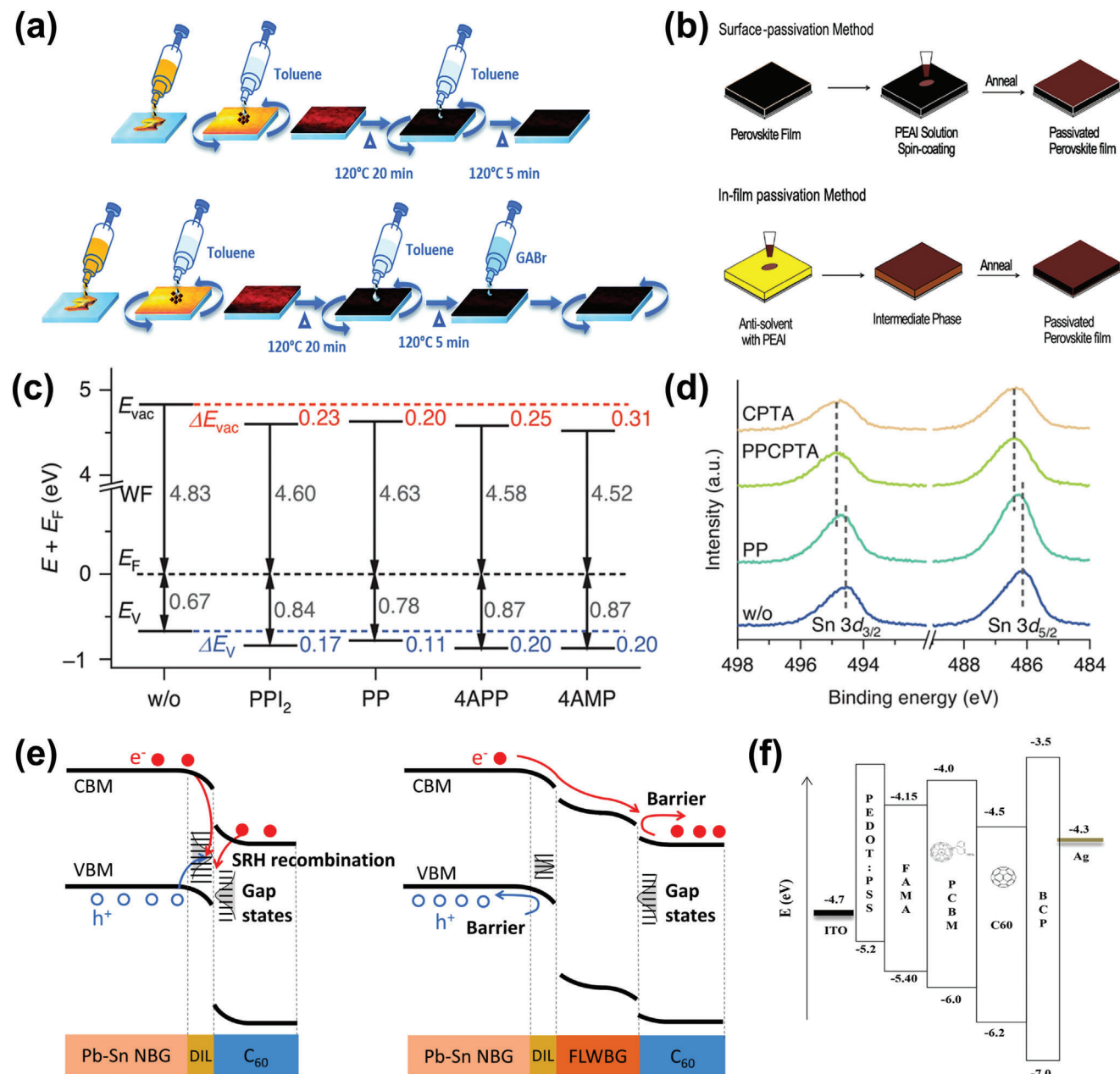
Figure 7. a) Schematic illustration of the fabrication steps for the control (upper panel) and GABr-treated (lower panel) perovskite films. Reproduced with permission.[110] Copyright 2020, The Royal Society of Chemistry. b) Schematic of surface and in situ passivation approaches to treat perovskite films. Reproduced with permission.[112] Copyright 2019, Wiley-VCH. c) Energy level diagrams and d) XPS spectra of Sn 3d2/3 and 3d5/2 core levels of Sn-Pb perovskite films without and with various post-treatment as indicated. E_{vac}: vacuum level; E_V: VBM; E_F: Fermi level. Reproduced with permission.[113] Copyright 2022, Wiley-VCH. e) Energy diagram of control and perovskite heterojunction Sn-Pb PSCs. The perovskite heterojunction helps to block holes (blue line) and extract electrons (red line) to minimize charge recombination at the defect interface layer. Reproduced with permission.[38] Copyright 2023, Springer Nature. f) Spike energy diagram of PCBM insertion. Reproduced with permission.[114] Copyright 2018, American Chemical Society.

followed by spin-coating organic salts FAI/FABr in isopropanol (IPA). As shown in Figure 7e, the energetic diagram of PSCs with and without heterojunction demonstrated that the Type II band alignment between the Sn-Pb perovskite and the WBG perovskite could substantially suppress the hole concentration, reduce the charge recombination in the defect interface layer, and facilitate the electron extraction from the perovskite to the C_{60} ETL. The

improved photoluminescence intensity of perovskite films and the improved built-in potential in heterojunction devices (from 0.724 to 0.775 V) suggest the reduction of nonradiative recombination losses and a wider depletion region for the bilayer heterojunction cells. The electroluminescence quantum yield improved from 0.47% to 3.09%, corresponding to a reduction of ≈50 mV for the V_{OC} loss. The TRPL lifetime also significantly increased, from
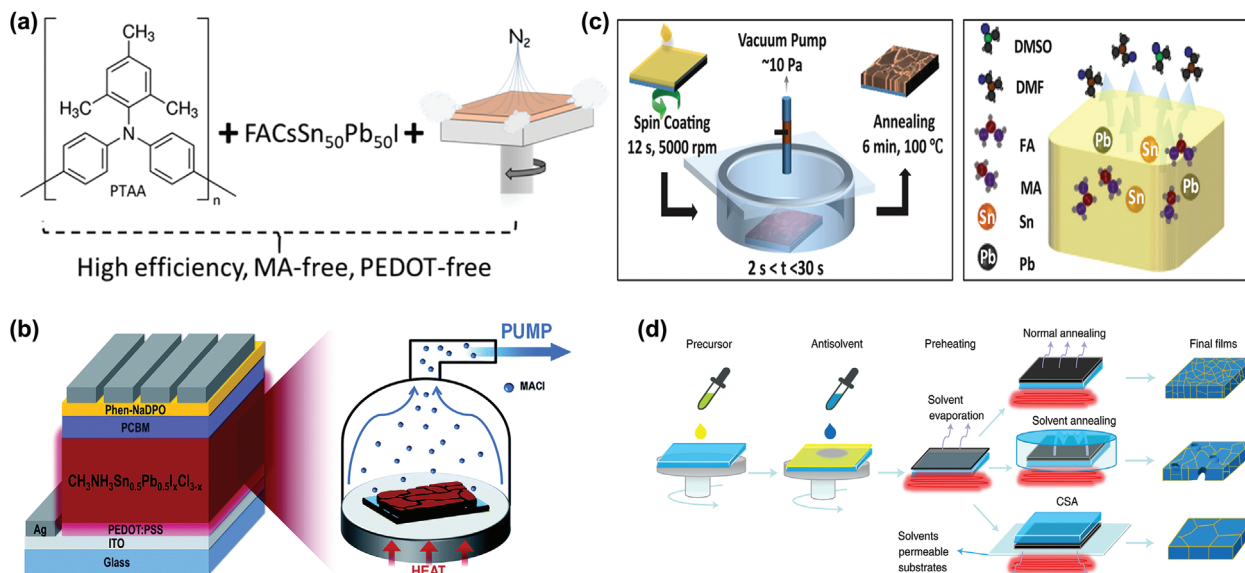
**ADVANCED
SCIENCE NEWS**

www.advancedsciencenews.com

**ADVANCED
MATERIALS**

www.advmat.de

Figure 8. a) Schematic of N_2 gas quenching of MA-free mixed Sn-Pb perovskites. Reproduced with permission.[45] Copyright 2020, American Chemical Society. b) Device architecture and schematic illustration of the VATA process. Reproduced with permission.[116] Copyright 2018, The Royal Society of Chemistry. c) Schematic illustration of the VAGC method for preparing Sn-Pb perovskite films. Reproduced with permission.[117] Copyright 2019, Wiley-VCH. d) Schematics of normal annealing, solvent annealing, and CSA processes for perovskite films. Reproduced with permission.[28] Copyright 2022, Springer Nature.

1073 to 3614 ns, and the device V_{OC} was improved to 0.873 V with a PCE of 23.8%. Owing to the effective blocking of the diffusion of oxygen from the 3D WBG perovskite layer, the heterojunction Sn-Pb PSCs sustained negligible degradation in the performance after aging over 3000 h in N_2-filled glovebox. By combining this heterojunction Sn-Pb perovskite with a 1.78-eV WBG perovskite, they achieved a certified stabilized efficiency of 28.5%, and the encapsulated device sustained 93% of its initial performance after 600-h MPP tracking in air.

Inspired by CIGS solar cell work, Hayase et al. introduced the concept of a spike energy structure by inserting a thin PCBM layer between the perovskite and C_{60} layers (Figure 7f).[114] The spike structure was shown to facilitate electron collection and hole blocking, leading to improved V_{OC}. Tuning the PCBM thickness was found to be critical to the V_{OC} and PCEs of Sn-Pb PSCs. In a follow-up study, Hayase et al. introduced an additional interlayer of ethylenediamine (EDA), a Lewis base, to change the p-type surface to an n-type for the Sn-Pb perovskite absorber layer.[115] This interlayer formed a graded-band structure by raising the Fermi energy level at the perovskite surface, increasing the built-in potential from 0.56 to 0.76 eV. In addition, the EDA interlayer reduced the defect density from the Sn^{2+} oxidation by preventing oxygen penetration and bonding with the undercoordinated Sn on the surface. With the additional role of the Br anion incorporation (2.5 mol% to I), the lattice strain and Urbach energy were both decreased, and the devices achieved 21.74% PCEs and 0.86-V V_{OC}.

3.4. Solvent Extraction Control

The rapid crystallization of the Sn-Pb perovskite precursor makes it challenging to control the film quality and microstructure of

Sn-Pb perovskites. It is critical to have key control of the solvent extraction and film annealing.

Werner et al. found wrinkle textures and poor crystal quality when using a mixed DMF/DMSO (4:1 in volume ratio) solvent for preparing Sn-Pb perovskites with a composition of $FA_{0.75}Cs_{0.25}Sn_{0.5}Pb_{0.5}I_3$ following the conventional antisolvent process.[45] To address this challenge, they employed the N_2 quenching method to replace the typical diethyl-ether antisolvent to enhance the quality of MA-free mixed Sn-Pb perovskite film prepared on PTAA HTL (**Figure 8a**). They found that the solvent of DMSO could be more sufficiently removed compared to the antisolvent treatment and generated a good uniform perovskite film without any wrinkle morphology. As a result, they achieved 17.5% and 20.0% PCEs on 1.0 and 0.06 cm^2, respectively. In addition, the devices sustained 80% of their initial performance after 4000 h at 85 °C in nitrogen by replacing the silver electrode with indium zinc oxide (IZO) to prevent the iodine-migration-induced degradation. The PTAA HTL helped to minimize humidity penetration, leading to improved stability.

Liu et al. demonstrated a vacuum-assisted (1000-Pa) thermal annealing (VATA) strategy to increase the coverage and crystallinity of the $MASn_{0.5}Pb_{0.5}I_xCl_{3-x}$ perovskite film.[116] The VATA strategy could quickly remove MACl in the perovskite precursor to produce pinhole-free film, which avoided the low-temperature sublimation of MACl in a working device (Figure 8b). In another study, Nejand et al. showed a similar vacuum-assisted growth control (VAGC) approach to avoid the antisolvent process.[117] As shown in Figure 8c, the rapid supersaturation of the wet film was promoted by employing 10-s vacuum (10 Pa); this resulted in the homogeneous removal of solvent to form a uniform perovskite thin film with large grains. The corresponding Sn-Pb perovskite film also exhibited reduced nonradiative recombination losses and improved carrier lifetime. As a result, the solar cells achieved
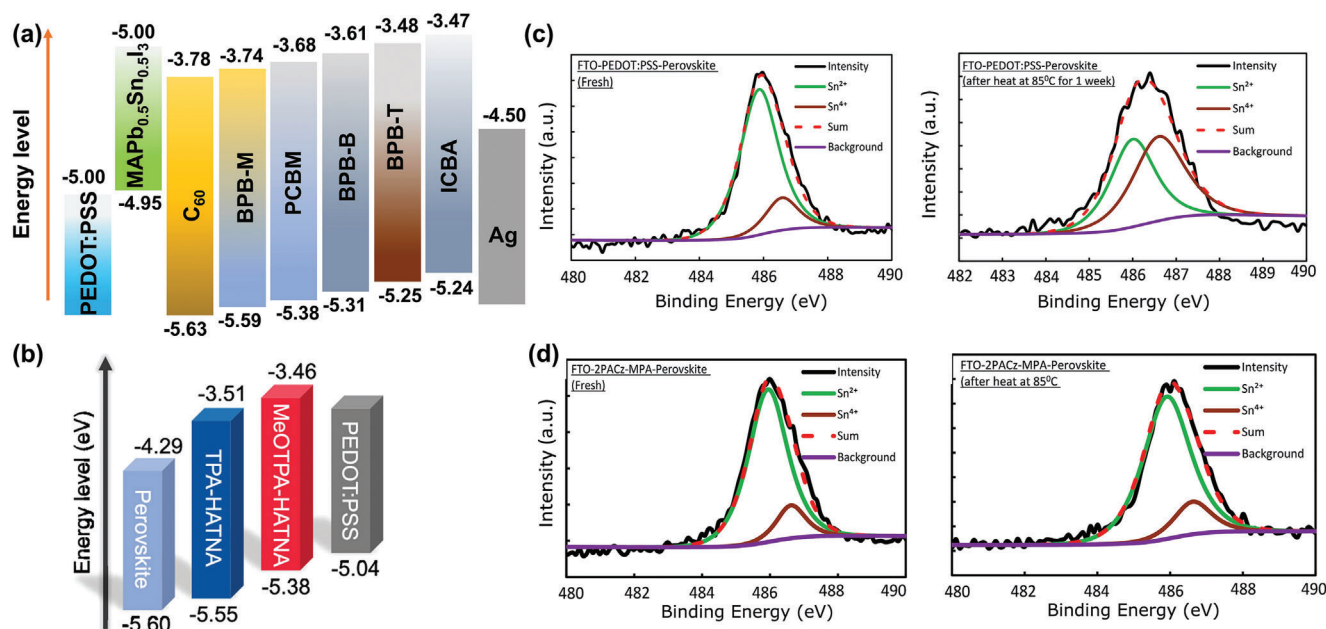
ADVANCED
SCIENCE NEWS

www.advancedsciencenews.com

ADVANCED
MATERIALS

www.advmat.de

Figure 9. a) Energy level diagram of PEDOT:PSS, Sn-Pb perovskite, and various ETMs based on C_{60} and its derivative materials. Reproduced with permission.[119] Copyright 2016, Elsevier. b) Comparison of energy levels between perovskites and various HTMs. Reproduced with permission.[120] Copyright 2022, American Chemical Society. c,d) XPS characterizations of fresh and aged (condition as indicated) Sn-Pb perovskite films using PEDOT:PSS or MPA/2PACz HTL on FTO substrates. Reproduced with permission.[47] Copyright 2022, American Chemical Society.

18.2% efficiency compared to the 15.4% efficiency of the antisolvent process device.

To control the crystallization of the Sn-Pb perovskite, Li et al. reported a close-space annealing (CSA) strategy by directly placing film side of the intermediate phase on solvent-permeable covers during annealing.[28] This CSA approach enabled the accurate control of the intermediate phase with residual solvent by preheating the film on a hot plate at 65 °C for a specific time, as shown in Figure 8d. With this approach, crystals were obtained with a grain size greater than 1 μm and a smooth surface compared to the typical annealing process, which generally yields 400 nm. The TRPL lifetime increased to 670 ns by using the CSA strategy compared to 204 ns using the typical annealing process. As a result, the V_{OC} improved from 0.830 to 0.857 V with an efficiency of 21.22%. Finally, they demonstrated 24.5% efficiency with 1.949-V V_{oc} by integrating the Sn-Pb NBG and 1.75-eV perovskites in a 2T all-perovskite tandem device.

3.5. Charge Transport Materials

Charge transport materials (CTMs), including both ETLs and HTLs, are important for developing high-performance Sn-Pb PSCs. For state-of-the-art Sn-Pb PSCs, C_{60} or its derivatives are commonly used as the ETL, and the HTL is normally poly(3,4-ethylenedioxy-thiophene):poly(styrene sulfonate) (PEDOT:PSS). Because PEDOT:PSS presents a challenge to the stability of Sn-Pb PSCs, there are efforts to replace PEDOE:PSS with poly[bis(4phenyl)(2,4,6trimethylphenyl)amine] (PTAA) or self-assembled monolayer (SAM) materials, such as 2PACz and Br-2PACz.

C_{60} and its fullerene derivative materials are the typical ETL for p-i-n PSCs, including Sn-Pb PSCs. A thin layer of C_{60} is normally coated on the perovskite surface by thermal evaporation to ensure conformal growth; however, it was reported that the energy mismatch between the LUMO of C_{60}[118] and Sn-Pb perovskites ($MASn_xPb_{1-x}I_3$)[43] can affect electron extraction (**Figure 9**a). Lin et al. reported a Frenkel-Wannier-Mott exciton hybridization of the $MASn_{0.5}Pb_{0.5}I_3$ perovskite.[119] In this study, three fullerene derivatives were synthesized—BPB-B, BPB-T, and BPB-M—with different LUMO levels (Figure 9a), and the V_{OC} of Sn-Pb PSCs was found to be affected by the LUMO of the ETL materials instead of the perovskite layer. The "spike" energy structure by inserting a thin PCBM layer between the Sn-Pb perovskite and the C_{60}, as demonstrated by Hayase et al., also represents an effective ETL modification to improve the V_{OC} by 60 mV.[114]

In contrast to ETL development, there is relatively more effort on HTL development for Sn-Pb PSCs. PEDOT:PSS is the most common HTL of highly efficient p-i-n structure Sn-Pb PSCs; however, the energy alignment between Sn-Pb perovskites and PEDOT:PSS is not ideal because of its relatively shallow LUMO. As an effort to address this challenge, Ning et al. reported that mixing a perfluorinated ionomer in PEDOT:PSS (volume ratio of 1:16) pushed the HTL LUMO from −5.02 to −5.19 eV, which reduced the energy mismatch between the Sn-Pb perovskite absorber ($FA_{0.6}MA_{0.4}Sn_{0.6}Pb_{0.4}I_3$) and the HTL for better hole extraction and higher V_{oc}.[121] In addition to tuning the LUMO, the surface modification of PEDOT:PSS has also been considered as an effective approach for better device performance because the hydrophilic properties of the PEDOT:PSS can create defect states and limit device operation. Zhang et al. introduced hydroquinone on the top of PEDOT:PSS before depositing the Sn-Pb perovskite $(MAPbI_3)_{0.7}(FASnI_3)_{0.3}$.[122] The change in the PEDOT:PSS

surface property improved the Sn-Pb perovskite quality with ≈1-μm grain size. Moreover, they found that the metallic property of PEDOT:PSS can cause an interfacial barrier limiting hole extraction, and the hydroquinone surface treatment can reduce the interfacial barrier for hole transport with a lower interfacial resistance and current leakage. Note that despite these efforts, the hydrophilic properties of PEDOT:PSS still present a challenge for device performance, especially operational stability. In addition, the parasitic absorption of PEDOT:PSS represents a critical limit in achieving high-current-density, all-perovskite tandem solar cells; thus, more efforts should focus on developing alternative HTL materials for Sn-Pb PSCs.

PTAA shows promise as a good alternative candidate for consideration to replace PEDOT:PSS because PTAA has been successfully demonstrated in pure Pb-based PSCs with good performance.[123–125] Using a two-step approach for perovskite deposition and PTAA as the HTL, Wang et al. reported the growth of $FA_{0.7}MA_{0.3}Sn_{0.3}Pb_{0.7}I_3$ perovskite film on PTAA with a large (>1-μm) grain size, increased perovskite crystallinity, reduced trap density, and reduced recombination losses.[126] As a result, the V_{OC} improved by 60 mV, and the device sustained 80% of its initial performance after 30-day storage in a glove box without encapsulation. McGehee et al. also employed PTAA by using N_2 quenching for an MA-free Sn-Pb perovskite ($FA_{0.75}Cs_{0.25}Sn_{0.5}Pb_{0.5}I_3$), which substantially improved the V_{OC} from 0.692 to 0.798 V with the PMMA treatment on the PTAA surface; as a result, the best efficiency reached 20% for the first time for MA-free Sn-Pb PSCs.[45] With the N_2 quenching, coupled with using IZO to replace Ag electrode, the devices maintained 80% of initial PCEs after 4000 h thermal stress in N_2, which further illustrated the value of PTAA in comparison to PEDOT:PSS for Sn-Pb PSCs.

Guo et al. found that hexaazatrinaphthylene (HATNA) could be a promising HTL for Sn-Pb PSCs.[120] In this study, triphenylamine (TPA) and methoxy-triphenylamine were introduced to the HATNA core to modify the molecular energy levels (Figure 9b), surface wettability, hole mobility, and thermal stability. The resulting Sn-Pb perovskite film showed reduced Sn^{2+} oxidation and vertically-oriented perovskite growth. The corresponding device exhibited an improved V_{OC} of 0.79 V compared to the 0.72 V based on PEDOT:PSS HTL. In addition, the TPA-HATNA-based Sn-Pb PSCs showed more than 50% improvement in the device stability under MPP tracking in air. The improved stability was attributed to the low solubility of TPA-HATNA in DMF/DMSO and its less acidic property compared to PEDOT:PSS.

In recent years, SAM HTL materials have attracted attention for developing highly efficient, pure Pb-based, single-junction as well as perovskite-Si tandem solar cells.[49,53,54] The ultrathin layer of SAM makes it attractive for excellent optical properties with essentially no parasitic absorption. Hole extraction also seems effective for these device applications; thus, there is a strong motivation to apply SAM HTL for Sn-Pb PSCs. Along this direction, Hayase et al. first employed the SAM of 2-(9H-carbazol-9-yl) ethyl] phosphonic acid (2PACz) in Sn-Pb-based ($Cs_{0.025}FA_{0.475}MA_{0.5}Sn_{0.5}Pb_{0.5}I_{2.925}Br_{0.075}$) PSCs.[47] In this study, Sn-Pb PSCs based on 2PACz HTL exhibited a similar performance to those based on PEDOT:PSS with a V_{OC} of 0.86 V and PCE of 21.37%. This study further demonstrated a bilayer HTL structure combining methyl phosphonic acid (MPA) with 2PACz (MPA/2PACz) by inserting the MPA layer between the perovskite and 2PACz layers. In this structure, MPA provides additional interface passivation, as evidenced by the longer TRPL lifetime. XPS analysis showed that the MPA/2PACz bilayer HTL is more effective at suppressing Sn^{2+} oxidation for improved stability after a 7-day heat treatment at 85 °C in N_2 owing to the acidic property associated with PEDOT:PSS (Figure 9c,d). Note that the bilayer MAP/2PACz HTL resulted in a demonstration of Sn-Pb PSC with a V_{OC} of 0.88 V and a PCE of 23.23%.

Other SAM HTL materials have also been reported in recent studies. Loi et al. demonstrated the use of 2-(3, 6-dibromo-9H-carbazol-9-yl) ethyl] phosphonic acid (Br-2PACz) to replace PEDOT:PSS for $Cs_{0.25}FA_{0.75}Sn_{0.5}Pb_{0.5}I_3$-based PSCs.[127] The use of Br-2PACz HTL increased the grain dimension up to an average size of 729 nm with better orientation toward to (100) and (200) planes. TRPL analysis also indicated reduced trap-assisted recombination and better charge carrier transfer for Br-2PACz-based PSCs than PEDOT:PSS-based ones. As a result, the V_{OC} of Br-2PACz-based PSCs improved to 0.81 V with a PCE of 19.51% compared to the 16.33% PCE for PEDOT:PSS-based devices.

For the development of Sn-Pb perovskites and solar cells, we have discussed various engineering approaches including additives, solvents engineering, interfacial engineering, solvent extraction control, and charge transport materials development. The main goal is to develop Sn-Pb perovskites with good optoelectronic properties including strong adsorption coefficient, fewer defects, and superior operational stability. The absorption edge of Sn-Pb bandgap perovskites is still generally weaker than that of Pb-based perovskites. Bowman et al. compared the optical properties of Pb and Sn-Pb perovskites.[128] It shows that the Sn-Pb perovskite has faster recombination rate, higher doping density, and Urbach energy compared to the pure-Pb perovskite. Thus, reducing the defect density represents an effective approach to increase absorption near the absorption edge region. This is also consistent with recent efforts on various engineering approaches (growth environment, solvent, additives, etc.) to minimize defect formation and improve Sn-Pb PSC performance.

During early stage of Sn-Pb perovskite development, the carrier mobility of Sn-Pb perovskites is generally smaller than pure-Pb perovskites; for example, ≈40 $cm^2(V\ s)^{-1}$ for pure-Pb perovskites and < 20 $cm^2\ (V\ s)^{-1}$ for Sn-Pb perovskites.[129] Carrier lifetime was also significantly limited to nanosecond or sub-nanosecond range.[85] This is largely caused by the high doping and defect densities in Sn-Pb perovskites due to the easy oxidation of Sn^{2+} and fast crystallization kinetics associated with Sn^{2+} precursor. During the past several years, significant improvements were reported by using various growth controls;[12–15,32,36–38,46,113] the carrier lifetime for Sn-Pb perovskite has reached ≈10 μs,[14,15] which is comparable to the state-of-the-art Pb-based perovskites. Thus, it appears that there is no fundamental limitation on the transport and recombination associated with the state-of-the-art Sn-Pb perovskites in comparison to Pb-based perovskites. However, there is still room for reducing the defect density and the Urbach energy for Sn-Pb perovskites.[9] Future advances in this direction can be expected to further improve

2314341 (13 of 21)

**ADVANCED
SCIENCE NEWS**

www.advancedsciencenews.com

**ADVANCED
MATERIALS**

www.advmat.de

the optoelectronic properties of Sn-Pb perovskite in comparison to Pb-based perovskites.

Note that it is known that the Sn-Pb perovskites are challenging to work with owing to the high doping and defect densities and fast Sn^{2+} crystallization kinetics. However, over the past several years, there have been significant advances in controlling defects and doping densities by using various growth controls, including additives, interfacial engineering, solvent engineering, solvent extraction control, and carrier transport materials replacement. These improvements lead to small V_{OC} deficit for Sn-Pb PSCs (e.g., 0.334 V), which is also comparable to the Pb-based PSCs (e.g., 0.33 V).[130] Despite these advances, Sn-Pb perovskite materials are still far more difficult to handle than Pb-based perovskites due to their sensitivity to the processing atmosphere (e.g., oxygen-free) and compatible solvents. Without proper control, the dark carrier density can easily reach over 10^{17} cm^{-3}.[14] In addition, the imbalanced crystallization between Sn^{2+} and Pb^{2+} can cause morphological defects and compositional nonuniformity at the microstructure scale. Moreover, the operational stability, especially at high temperatures (e.g., 65 °C or higher) represents a key challenge that may hinder Sn-Pb PSC development.

The stability of Sn-Pb PSCs can be affected by multiple factors. The oxidation of Sn^{2+} is generally considered a prime culprit of Sn-Pb PSC degradation because Sn^{2+} can be oxidized to Sn^{4+}, resulting in defect formation and worse photocarriers dynamics. The common use of PEDOT:PSS as the HTL is another weakness for developing stable Sn-Pb PSCs. We have recently shown that the electrochemical redox reaction across the TCO/HTL/perovskite interface is important for Pb-based PSCs.[131] The interfacial electrochemical redox reaction can be even more complicated for Sn-Pb PSCs because of the mixed Sn^{2+} and Pb^{2+} chemistry. The reaction behavior at elevated temperatures could strongly affect the stability of Sn-Pb PSCs at high operational temperatures (e.g., 65 °C or higher). In addition to these factors that are directly related to Sn-Pb PSCs, the factors that are common to Pb-based PSCs are also expected to be applicable to Sn-Pb PSCs. For example, Mundt et al. showed that the stability of Sn-Pb perovskite films is also affected by the formation of I_3^- intermediates proceeding I_2 loss from the decomposition of MA$^+$ at the surface and evidence of under-coordinated Sn and Pb surface sites ($Sn^{\delta<2+}$ and $Pb^{\delta<2+}$, respectively) in inert and ambient conditions.[132]

To improve operational stability of Sn-Pb PSCs, various engineering approaches can be used to suppress Sn^{2+} oxidation and defect states, and enhance carrier lifetimes. In addition, improvements in alternative HTLs and electrochemical properties at the TCO/HTL/Sn-Pb perovskite interface are also critical to Sn-Pb PSC long-term operation, especially at high temperatures. Moreover, device encapsulation (oxygen-free environment) is expected to be more critical for Sn-Pb PSCs than for the Pb-based counterpart. Finally, we note that in comparison to Pb-based perovskites, Sn-Pb perovskites are easier to form defects related to Sn^{2+} oxidation, which can easily happen from perovskite precursor ink preparation to the post-thermal treatment of perovskite films as well as during device operation at high temperatures. Thus, we also need to consider new solvent systems with strong interaction with the perovskite components, superior thermal stability, good solubility, and suppressed Sn^{2+} oxidation.

4. Application in 2T All-Perovskite Tandem Solar Cells

With the effort in recent years, the performance of single-junction Sn-Pb PSCs has reached over 23%.[38,46,47,108] Although further improvement is expected based on discussions in the previous sections, reaching over 23% PCE for the NBG Sn-Pb PSCs is expected, in theory, to enable tandem devices reach over 30% when paired with high-quality WBG top cells.[133] Indeed, we have seen significant advances made in recent years on tandem devices based on Sn-Pb NBG perovskite subcells. Here, we focus on the 2T monolithic configuration of an all-perovskite tandem combining an Sn-Pb-based NBG bottom cell and a Pb-based WBG top cell; this approach represents a promising thin-film PV technology to reach ultrahigh PCEs with a low manufacturing cost.[12–14,29,31,32,36–39,112,134–145] Recent progress on all-perovskite 2T tandem development is summarized in Table S3, Supporting Information and **Figure 10a**; the best certified PCE has reached 29.1%.[48]

To obtain highly efficient 2T all-perovskite tandem solar cells, the combination of bandgaps should be ≈1.2 eV for the bottom cell and ≈1.8 eV for the top cell,[26] as shown in Figure 10b. For the tandem device, the incident light first passes through the WBG top cell, with most of the light in the short-wavelength range being absorbed, and the remaining long-wavelength range is absorbed by the NBG Sn-Pb bottom cell. In the initial all-perovskite tandem study, Snaith et al. reported the combination of an ≈1.2-eV $FA_{0.75}Cs_{0.25}Sn_{0.5}Pb_{0.5}I_3$ NBG perovskite and an ≈1.8-eV $FA_{0.83}Cs_{0.17}Pb(I_{0.5}Br_{0.5})_3$ perovskite, demonstrating 17% tandem PCE with a current density of 14.5 mA cm^{-2}. A key to the successful demonstration of the 2T all-perovskite tandem is to add a buffer layer of tin oxide (SnO_2) and zinc tin oxide on top of the top perovskite subcell before depositing the ITO recombination layer to enable solution processing of the bottom perovskite subcell. In subsequent years, a thin metal layer (≈1 nm, Ag or Au) was adopted as the recombination layer in 2T all-perovskite tandem architectures, showing significantly improved tandem performance.[35,36]

The progress of all-perovskite tandem devices has been accompanied by subcell development. During the early stages, the NBG Sn-Pb perovskite subcell limited the 2T tandem performance; thus, significant effort was made to improve Sn-Pb perovskites with reduced Sn^{2+} oxidation, longer carrier lifetime, and improved film morphology, as discussed in previous sections. As the quality of NBG Sn-Pb perovskites has improved, the performance of mixed Sn-Pb PSCs has also improved to 18.1% with a V_{OC} of 0.84 V; as a result, the PCE of all-perovskite tandems has improved to more than 20% for the first time.[35] The performance of all-perovskite 2T tandems later exceeded 26% when the thickness of mixed Sn-Pb perovskite films increased to ≈1.2 μm with the assistance of using 4-trifluoromethyl-phenylammonium as a surface passivator to enable long carrier diffusion length (Figure 10c).[32] As a result, the J_{SC} of all-perovskite 2T tandem solar cells was improved to 16.5 mA cm^{-2} with a certified PCE of 26.4%. With the advances in Sn-Pb perovskites pushing 2T all-perovskite tandems to a new stage, the V_{OC} of all-perovskite tandems started to limit further advances in tandem performance. This is mainly caused by the halide-segregation of the Br-I mixed-halide WBG perovskite causing a serious V_{OC}
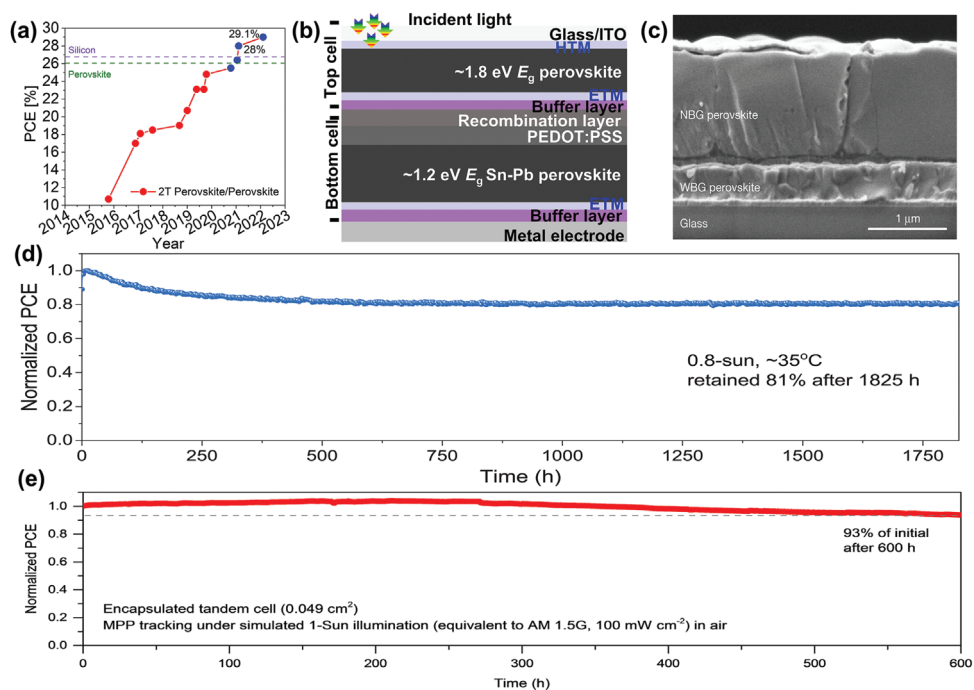
Figure 10. a) Progress of 2T all-perovskite tandem solar cells. Green dotted line: 26.1% PCE of single-junction PSCs; purple dotted line: 26.81% PCE of single-junction Si solar cells. b) Schematic of 2T all-perovskite tandem configuration. c) Cross-sectional SEM image of a typical 2T all-perovskite tandem solar cell. Reproduced with permission.[143] Copyright 2023, Wiley-VCH. d) Long-term stability tracking of an unencapsulated 2T all-perovskite tandem device under continuous light illumination in N_2. Reproduced with permission.[145] Copyright 2022, AAAS. e) MPP tracking of an encapsulated 2T all-perovskite tandem device under simulated AM 1.5G illumination in air with 30–50% humidity. Reproduced with permission.[38] Copyright 2023, Nature Springer.

deficit of the WBG top cell when the bandgap is greater than 1.7 eV.[146] More effort has been directed to address this issue in recent years. For example, a recent study showed that the V_{OC} of all-perovskite tandem solar cells increased to 2.10 V by using the surface treatment of 1,3-propane diammonium to improve WBG perovskites.[29] Yang et al. developed a triple-halide WBG perovskite and employed piperazinium iodide as a surface modification agent, which improved the V_{OC} of WBG PSC and the corresponding 2T tandem to 1.36 and 2.154 V, respectively; the tandem also reached a certified efficiency of 27.5%.[143] Jiang et al. introduced compositional textured engineering by coupling a gentle gas quenching with a high-Br-content WBG perovskite to enable a columnar growth of WBG perovskite film with significantly reduced defect density at grain boundaries. As a result, the 1.75-eV mixed-halide WBG PSC displayed a V_{OC} of 1.33 V, and when integrated with a 1.25-eV NBG PSC, the V_{OC} of a 2T tandem increased to 2.2 V.[145]

With the rapid efficiency progress of all-perovskite 2T tandem cells, the corresponding stability performance has also significantly improved. In a recent study, a mixture of PEAI and GuaSCN was jointly introduced to the mixed Sn-Pb perovskite precursor, leading to the formation of a quasi-2D structure $(PEA)_2GAPb_2I_7$ at the grain boundary and surface of the $(FASnI_3)_{0.6}(MAPbI_3)_{0.4}$ Sn-Pb perovskite thin film.[14] This quasi-2D structure helped improve the operational stability of Sn-Pb single-junction PSCs by retaining more than 82% of its maximum efficiency after 1830-h operation under simulated solar illumination in N_2. Similarly, the corresponding 2T tan-

dem device maintained 80% of its maximum efficiency after 1500-h operation.[14] With the compositional texture engineering strategy to further improve the WBG top cell, the unencapsulated 2T tandem device sustained 81% of its maximum efficiency after ≈1825-h operation at 0.8 suns in N_2 (Figure 10d). In a recent study by Tan et al., the 3D/3D bilayer perovskite heterojunction structure not only pushed the single-junction NBG Sn-Pb PSC to 23.8% and certified 2T tandem to 28.0% but also increased the stability of the resulting 2T tandem device, demonstrating T93 of 600 h for an encapsulated device under MPP tracking in air with 30–50% relative humidity (Figure 10e).[38]

With the continuous improvement in both the efficiency and stability of all-perovskite tandem solar cells, upscaling for tandem module development has slowly become a key challenge for future commercialization. Nejand et al. used blade coating coupled with vacuum deposition to prepare large-area coating of both NBG and WBG perovskite films for 2T all-perovskite tandem modules; the tandem module patterning was achieved using the standard laser scribing technique (**Figure 11a**).[141] Light-beam-induced-current (LBIC) mapping was employed to evaluate the homogeneity of the generated photocurrent for each subcell within the module. In addition, electroluminescence imaging was used to analyze the defect distribution of each subcell by using a long-pass filter (≈760 nm) and a short-pass filter (≈775 nm) for imaging the bottom and top subcells, respectively (Figure 11b). With scalable deposition approaches, a tandem module with an aperture area of 12.25 cm^2 and

**ADVANCED
SCIENCE NEWS**

www.advancedsciencenews.com

**ADVANCED
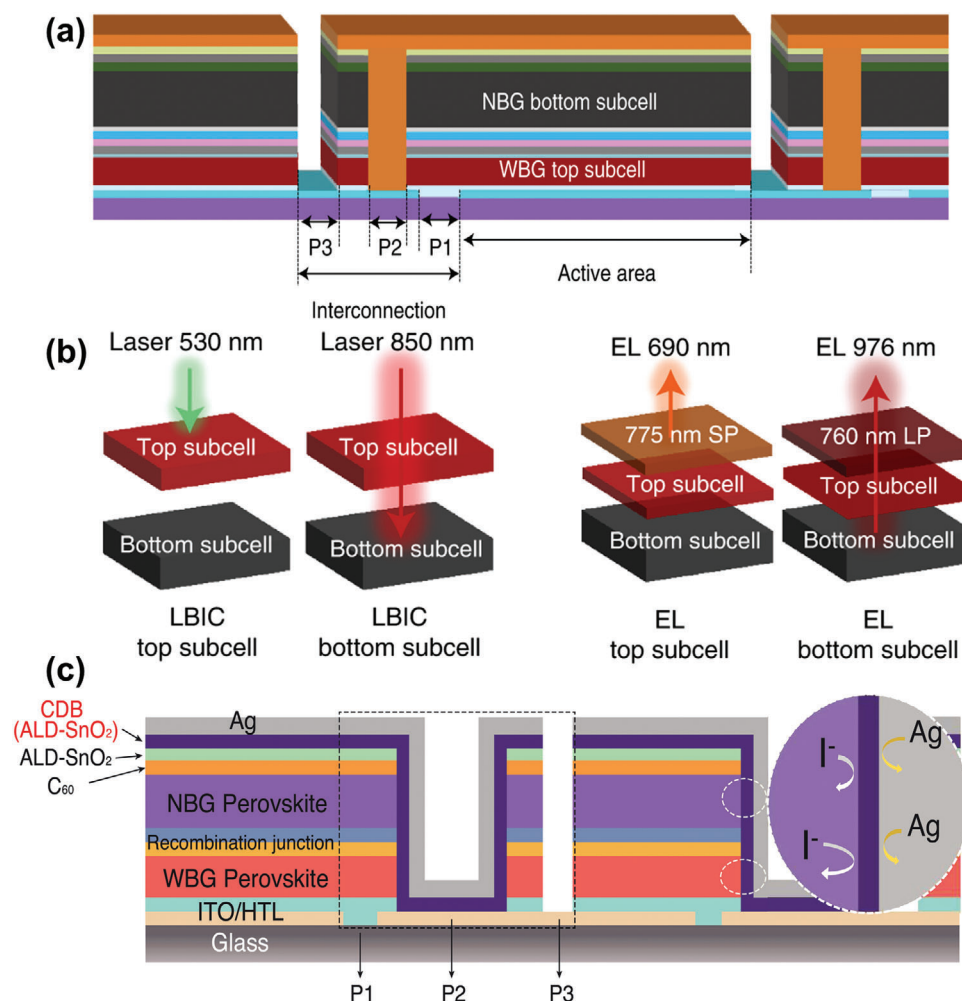MATERIALS**

www.advmat.de

Figure 11. a) Schematic illustrations of the active area and laser scribing lines for 2T all-perovskite tandem module b) as well as the laser excitation for measuring the LBIC signal (left two panels) and electroluminescent images with different optical bypass filters (right two panels). Reproduced with permission.[141] Copyright 2022, Nature Springer. c) Schematic illustration of the CDB layer to prevent interdiffusion in a 2T all-perovskite tandem module. Reproduced with permission.[144] Copyright 2022, AAAS.

geometric fill factor of 94.7% reached an aperture efficiency of 19.1%. Similarly, Tan et al. also reported the use of blade coating to prepare both the NBG and WBG perovskite thin films over a large substrate area for 2T all-perovskite tandem module development.[144] Systematically tuning the Cs ratio in the WBG perovskite composition was critical to ensuring the uniform crystallization of 1.8-eV WBG perovskite thin films. The Ag metal contact was found to significantly affect the module stability because of the halide-metal electrode reaction between the perovskite and Ag in the P2 scribed region (Figure 11c). To address this challenge, ≈10 nm of ALD-SnO$_x$ was conducted after P2 scribing as a conformal diffusion barrier (CDB) to prevent reaction and interdiffusion between the perovskite material and the Ag electrode. As a result, they obtained 22.5% efficiency with an aperture area of 20.25 cm^2 for an all-perovskite tandem module. The encapsulated modules sustained 75% of their initial efficiency after MPP tracking over 500 h in the air under simulated AM 1.5-G illumination.[144]

5. Conclusion and Outlook

In this review, first, we summarized the progress of Sn-Pb perovskites with respect to the unique bowing effect and the origin of unstable mechanisms of Sn-Pb perovskites. We also highlighted recent advances on various strategies to improve Sn-Pb PSCs, such as additive engineering, solvent tuning, interface modification, solvent extraction control, and CTM development. Understanding the mechanisms of these various strategies is critical to further advancing Sn-Pb PSCs, especially related to suppressing Sn^{2+} oxidation, defect density, and nonradiative recombination losses and to improving the stability and efficiency of Sn-Pb PSCs. In particular, the design and development of new CTMs to replace the conventional PEDOT:PSS HTL represent the most critical task to enable a wider range of device stack designs with robust stability, especially at elevated operational temperatures. We also reviewed the application of Sn-Pb perovskites as the bottom subcell in 2T all-perovskite tandem solar cells along with

**ADVANCED
SCIENCE NEWS**

www.advancedsciencenews.com

**ADVANCED
MATERIALS**

www.advmat.de

recent progress on reducing the voltage deficit in the WBG PSCs to improve 2T tandem voltage output.

To further improve the performance of all-perovskite tandem solar cells, the J_{SC} of tandem devices should be improved by increasing the single-junction current density of Sn-Pb perovskite subcells. At present, the state-of-art J_{SC} of all-perovskite tandem devices is still limited by the Sn-Pb perovskite subcell, which is ≈33 mA cm^{-2}. There is still significant room for further improvement of J_{SC} to reach ≈90% of the SQ limit for mixed Sn-Pb NBG PSCs (Figure 2b). This can be achieved by using a thicker Sn-Pb perovskite film and minimizing the parasitic absorption by replacing PEDOT:PSS along with other optical management tailored for the tandem architecture.

The operational stability of tandem solar cells is often worse than the single-junction subcells, suggesting that the integration component (e.g., the interconnection layer) might be a limiting component on stability; therefore, it is critical to carry out systematic investigations to compare the stability of single-junction and tandem devices. Understanding the degradation mechanisms and their differences is valuable to the tandem community. Note that for Sn-Pb PSCs, the stability seems especially challenging at an elevated temperature (e.g., >65 °C) compared to pure Pb-based PSCs. Whether this is related to the intrinsic material properties of Sn-Pb perovskites or to the device contact layer, such as the acidic and hydrophilic PEDOT:PSS, remains to be answered with further studies.

Many research groups currently use conventional spin coating for preparing high-performance tandem solar cells; however, spin coating is not scalable and should be transitioned to blade or slot-die for solution processing. It is expected that many research groups will make such a transition as the perovskite PV technologies get closer to the marketplace. Meanwhile, the upscaling design of the module for all-perovskite tandem solar cell should be considered with respect to the potential thermal damage caused during laser scribing for module fabrication. In addition, scribing passivation should become a key point separating the module-level and cell-level device operation over a long period of time. With all these future studies and developments, the potential of Sn-Pb perovskite single-junction and all-perovskite tandem solar cells is expected to be realized with better performance and stability at a large scale for practical applications.

Supporting Information

Supporting Information is available from the Wiley Online Library or from the author.

Acknowledgements

Conflict of Interest

The authors declare no conflict of interest.

Keywords
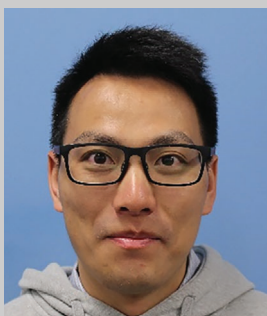
[1] A. Kojima, K. Teshima, Y. Shirai, T. Miyasaka, *J. Am. Chem. Soc.* **2009**, *131*, 6050.

[2] National Renewable Energy Laboratory, http://www.nrel.gov/ncpv/images/efficiencychart.jpg (accessed: December 2023).

[3] S. De Wolf, J. Holovsky, S. J. Moon, P. Loper, B. Niesen, M. Ledinsky, F. J. Haug, J. H. Yum, C. Ballif, *J. Phys. Chem. Lett.* **2014**, *5*, 1035.

[4] Q. Dong, Y. Fang, Y. Shao, P. Mulligan, J. Qiu, L. Cao, J. Huang, *Science* **2015**, *347*, 967.

[5] J. Burschka, N. Pellet, S. J. Moon, R. Humphry-Baker, P. Gao, M. K. Nazeeruddin, M. Gratzel, *Nature* **2013**, *499*, 316.

[6] N. J. Jeon, J. H. Noh, W. S. Yang, Y. C. Kim, S. Ryu, J. Seo, S. I. Seok, *Nature* **2015**, *517*, 476.

[7] G. Xing, N. Mathews, S. S. Lim, N. Yantara, X. Liu, D. Sabba, M. Gratzel, S. Mhaisalkar, T. C. Sum, *Nat. Mater.* **2014**, *13*, 476.

[8] D. P. McMeekin, G. Sadoughi, W. Rehman, G. E. Eperon, M. Saliba, M. T. Hörantner, A. Haghighirad, N. Sakai, L. Korte, B. Rech, M. B. Johnston, L. M. Herz, H. J. Snaith, *Science* **2016**, *351*, 151.

[9] B. Subedi, C. Li, C. Chen, D. Liu, M. M. Junda, Z. Song, Y. Yan, N. J. Podraza, *ACS Appl. Mater. Interfaces* **2022**, *14*, 7796.

[10] S. D. Stranks, G. E. Eperon, G. Grancini, C. Menelaou, M. J. P. Alcocer, T. Leijtens, L. M. Herz, A. Petrozza, H. J. Snaith, *Science* **2013**, *342*, 341.

[11] C. Wehrenfennig, G. E. Eperon, M. B. Johnston, H. J. Snaith, L. M. Herz, *Adv. Mater.* **2014**, *26*, 1584.

[12] Z. Yang, Z. Yu, H. Wei, X. Xiao, Z. Ni, B. Chen, Y. Deng, S. N. Habisreutinger, X. Chen, K. Wang, J. Zhao, P. N. Rudd, J. J. Berry, M. C. Beard, J. Huang, *Nat. Commun.* **2019**, *10*, 4498.

[13] J. Tong, Z. Song, D. H. Kim, X. Chen, C. Chen, A. F. Palmstrom, P. F. Ndione, M. O. Reese, S. P. Dunfield, O. G. Reid, J. Liu, F. Zhang, S. P. Harvey, S. Li, S. T. Christensen, G. Teeter, D. Zhao, M. M. Al-Jassim, M. F. A. M. van Hest, M. C. Beard, S. E. Shaheen, J. J. Berry, Y. Yan, K. Zhu, *Science* **2020**, *346*, 475.

[14] J. Tong, Q. Jiang, A. J. Ferguson, A. F. Palmstrom, X. Wang, J. Hao, S. P. Dunfield, A. E. Louks, S. P. Harvey, C. Li, H. Lu, R. M. France, S. A. Johnson, F. Zhang, M. Yang, J. F. Geisz, M. D. McGehee, M. C. Beard, Y. Yan, D. Kuciauskas, J. J. Berry, K. Zhu, *Nat. Energy* **2022**, *7*, 642.

[15] F. Yang, R. W. MacQueen, D. Menzel, A. Musiienko, A. Al-Ashouri, J. Thiesbrummel, S. Shah, K. Prashanthan, D. Abou-Ras, L. Korte, M. Stolterfoht, D. Neher, I. Levine, H. Snaith, S. Albrecht, *Adv. Energy Mater.* **2023**, *13*, 2204339.

[16] S.-H. Turren-Cruz, A. Hagfeldt, M. Saliba, *Science* **2018**, *362*, 449.

[17] Z. Wei, K. Yan, H. Chen, Y. Yi, T. Zhang, X. Long, J. Li, L. Zhang, J. Wang, S. Yang, *Energy Environ. Sci.* **2014**, *7*, 3326.

**ADVANCED
SCIENCE NEWS**

www.advancedsciencenews.com

**ADVANCED
MATERIALS**

www.advmat.de

[18] C. Yan, J. Yu, Y. Li, P. W. K. Fong, R. Ding, K. Liu, H. Xia, Z. Ren, X. Lu, J. Hao, G. Li, *Matter* **2022**, *5*, 2238.

[19] L. Etgar, P. Gao, Z. Xue, Q. Peng, A. K. Chandiran, B. Liu, M. K. Nazeeruddin, M. Gratzel, *J. Am. Chem. Soc.* **2012**, *134*, 17396.

[20] M. M. Lee, J. Teuscher, T. Miyasaka, T. N. Murakami, H. J. Snaith, *Science* **2012**, *338*, 643.

[21] V. D'Innocenzo, G. Grancini, M. J. Alcocer, A. R. Kandada, S. D. Stranks, M. M. Lee, G. Lanzani, H. J. Snaith, A. Petrozza, *Nat. Commun.* **2014**, *5*, 3586.

[22] Q. Lin, A. Armin, R. C. R. Nagiri, P. L. Burn, P. Meredith, *Nat. Photonics* **2014**, *9*, 106.

[23] A. Miyata, A. Mitioglu, P. Plochocka, O. Portugall, J. T.-W. Wang, S. D. Stranks, H. J. Snaith, R. J. Nicholas, *Nat. Phys.* **2015**, *11*, 582.

[24] W. Shockley, H. J. Queisser, *J. Appl. Phys.* **1961**, *32*, 510.

[25] J. Im, C. C. Stoumpos, H. Jin, A. J. Freeman, M. G. Kanatzidis, *J. Phys. Chem. Lett.* **2015**, *6*, 3503.

[26] G. E. Eperon, T. Leijtens, K. A. Bush, R. Prasanna, T. Green, J. T. Wang, D. P. McMeekin, G. Volonakis, R. L. Milot, R. May, A. Palmstrom, D. J. Slotcavage, R. A. Belisle, J. B. Patel, E. S. Parrott, R. J. Sutton, W. Ma, F. Moghadam, B. Conings, A. Babayigit, H.-G. Boyen, S. Bent, F. Giustino, L. M. Herz, M. B. Johnston, M. D. McGehee, H. J. Snaith, *Science* **2016**, *354*, 861.

[27] R. He, W. Wang, Z. Yi, F. Lang, C. Chen, J. Luo, J. Zhu, J. Thiesbrummel, S. Shah, K. Wei, Y. Luo, C. Wang, H. Lai, H. Huang, J. Zhou, B. Zou, X. Yin, S. Ren, X. Hao, L. Wu, J. Zhang, J. Zhang, M. Stolterfoht, F. Fu, W. Tang, D. Zhao, *Nature* **2023**, *618*, 80.

[28] C. Wang, Y. Zhao, T. Ma, Y. An, R. He, J. Zhu, C. Chen, S. Ren, F. Fu, D. Zhao, X. Li, *Nat. Energy* **2022**, *7*, 744.

[29] H. Chen, A. Maxwell, C. Li, S. Teale, B. Chen, T. Zhu, E. Ugur, G. Harrison, L. Grater, J. Wang, S. Wang, L. Zeng, S. M. Park, L. Chen, P. Serles, R. A. Awni, B. Subedi, X. Zheng, C. Xiao, N. J. Podraza, T. Filleter, C. Liu, Y. Yang, J. M. Luther, S. De Wolf, M. G. Kanatzidis, Y. Yan, E. H. Sargent, *Nature* **2023**, *613*, 676.

[30] Z. Yu, Z. Yang, Z. Ni, Y. Shao, B. Chen, Y. Lin, H. Wei, Z. J. Yu, Z. Holman, J. Huang, *Nat. Energy* **2020**, *5*, 657.

[31] L. Li, Y. Wang, X. Wang, R. Lin, X. Luo, Z. Liu, K. Zhou, S. Xiong, Q. Bao, G. Chen, Y. Tian, Y. Deng, K. Xiao, J. Wu, M. I. Saidaminov, H. Lin, C.-Q. Ma, Z. Zhao, Y. Wu, L. Zhang, H. Tan, *Nat. Energy* **2022**, *7*, 708.

[32] R. Lin, J. Xu, M. Wei, Y. Wang, Z. Qin, Z. Liu, J. Wu, K. Xiao, B. Chen, S. M. Park, G. Chen, H. R. Atapattu, K. R. Graham, J. Xu, J. Zhu, L. Li, C. Zhang, E. H. Sargent, H. Tan, *Nature* **2022**, *603*, 73.

[33] Y. Wang, R. Lin, X. Wang, C. Liu, Y. Ahmed, Z. Huang, Z. Zhang, H. Li, M. Zhang, Y. Gao, H. Luo, P. Wu, H. Gao, X. Zheng, M. Li, Z. Liu, W. Kong, L. Li, K. Liu, M. I. Saidaminov, L. Zhang, H. Tan, *Nat. Commun.* **2023**, *14*, 1819.

[34] D. Zhao, Y. Yu, C. Wang, W. Liao, N. Shrestha, C. R. Grice, A. J. Cimaroli, L. Guan, R. J. Ellingson, K. Zhu, X. Zhao, R.-G. Xiong, Y. Yan, *Nat. Energy* **2017**, *2*, 17018.

[35] D. Zhao, C. Chen, C. Wang, M. M. Junda, Z. Song, C. R. Grice, Y. Yu, C. Li, B. Subedi, N. J. Podraza, X. Zhao, G. Fang, R.-G. Xiong, K. Zhu, Y. Yan, *Nat. Energy* **2018**, *3*, 1093.

[36] R. Lin, K. Xiao, Z. Qin, Q. Han, C. Zhang, M. Wei, M. I. Saidaminov, Y. Gao, J. Xu, M. Xiao, A. Li, J. Zhu, E. H. Sargent, H. Tan, *Nat. Energy* **2019**, *4*, 864.

[37] K. Xiao, R. Lin, Q. Han, Y. Hou, Z. Qin, H. T. Nguyen, J. Wen, M. Wei, V. Yeddu, M. I. Saidaminov, Y. Gao, X. Luo, Y. Wang, H. Gao, C. Zhang, J. Xu, J. Zhu, E. H. Sargent, H. Tan, *Nat. Energy* **2020**, *5*, 870.

[38] R. Lin, Y. Wang, Q. Lu, B. Tang, J. Li, H. Gao, Y. Gao, H. Li, C. Ding, J. Wen, P. Wu, C. Liu, S. Zhao, K. Xiao, Z. Liu, C. Ma, Y. Deng, L. Li, F. Fan, H. Tan, *Nature* **2023**, *620*, 994.

[39] T. Li, J. Xu, R. Lin, S. Teale, H. Li, Z. Liu, C. Duan, Q. Zhao, K. Xiao, P. Wu, B. Chen, S. Jiang, S. Xiong, H. Luo, S. Wan, L. Li, Q. Bao, Y. Tian, X. Gao, J. Xie, E. H. Sargent, H. Tan, *Nat. Energy* **2023**, *8*, 610.

[40] J. Tong, Z. Song, D. H. Kim, X. Chen, C. Chen, A. F. Palmstrom, P. F. Ndione, M. O. Reese, S. P. Dunfield, O. G. Reid, J. Liu, F. Zhang, S. P. Harvey, Z. Li, S. T. Christensen, G. Teeter, D. Zhao, M. M. Al-Jassim, M. van Hest, M. C. Beard, S. E. Shaheen, J. J. Berry, Y. Yan, K. Zhu, *Science* **2019**, *364*, 475.

[41] Q. Jiang, J. Tong, Y. Xian, R. A. Kerner, S. P. Dunfield, C. Xiao, R. A. Scheidt, D. Kuciauskas, X. Wang, M. P. Hautzinger, R. Tirawat, M. C. Beard, D. P. Fenning, J. J. Berry, B. W. Larson, Y. Yan, K. Zhu, *Nature* **2022**, *611*, 278.

[42] E. Jokar, C. H. Chien, C. M. Tsai, A. Fathi, E. W. Diau, *Adv. Mater.* **2019**, *31*, 1804835.

[43] F. Hao, C. C. Stoumpos, R. P. Chang, M. G. Kanatzidis, *J. Am. Chem. Soc.* **2014**, *136*, 8094.

[44] F. Zuo, S. T. Williams, P. W. Liang, C. C. Chueh, C. Y. Liao, A. K. Jen, *Adv. Mater.* **2014**, *26*, 6454.

[45] J. Werner, T. Moot, T. A. Gossett, I. E. Gould, A. F. Palmstrom, E. J. Wolf, C. C. Boyd, M. F. A. M. van Hest, J. M. Luther, J. J. Berry, M. D. McGehee, *ACS Energy Lett.* **2020**, *5*, 1215.

[46] S. Hu, K. Otsuka, R. Murdey, T. Nakamura, M. A. Truong, T. Yamada, T. Handa, K. Matsuda, K. Nakano, A. Sato, K. Marumoto, K. Tajima, Y. Kanemitsu, A. Wakamiya, *Energy Environ. Sci.* **2022**, *15*, 2096.

[47] G. Kapil, T. Bessho, Y. Sanehira, S. R. Sahamir, M. Chen, A. K. Baranwal, D. Liu, Y. Sono, D. Hirotani, D. Nomura, K. Nishimura, M. A. Kamarudin, Q. Shen, H. Segawa, S. Hayase, *ACS Energy Lett.* **2022**, *7*, 966.

[48] M. A. Green, E. D. Dunlop, M. Yoshita, N. Kopidakis, K. Bothe, G. Siefer, X. Hao, *Prog. Photovoltaics* **2023**, *31*, 651.

[49] A. Al-Ashouri, E. Köhnen, B. Li, A. Magomedov, H. Hempel, P. Caprioglio, J. A. Márquez, A. B. M. Vilches, E. Kasparavicius, J. A. Smith, N. Phung, D. Menzel, M. Grischek, L. Kegelmann, D. Skroblin, C. Gollwitzer, T. Malinauskas, M. Jošt, G. Matič, B. Rech, R. Schlatmann, M. Topič, L. Korte, A. Abate, B. Stannowsk, D. Neher, M. Stolterfoht, T. Unold, V. Getautis, S. Albrecht, *Science* **2020**, *370*, 1300.

[50] P. Tockhorn, J. Sutter, A. Cruz, P. Wagner, K. Jager, D. Yoo, F. Lang, M. Grischek, B. Li, J. Li, O. Shargaieva, E. Unger, A. Al-Ashouri, E. Kohnen, M. Stolterfoht, D. Neher, R. Schlatmann, B. Rech, B. Stannowski, S. Albrecht, C. Becker, *Nat. Nanotechnol.* **2022**, *17*, 1214.

[51] J. Liu, M. De Bastiani, E. Aydin, G. T. Harrison, Y. Gao, R. R. Pradhan, M. K. Eswaran, M. Mandal, W. Yan, A. Seitkhan, M. Babics, A. S. Subbiah, E. Ugur, F. Xu, L. Xu, M. Wang, A. ur Rehman, A. Razzaq, J. Kang, R. Azmi, A. Ali Said, F. H. Isikgor, T. G. Allen, D. Andrienko, U. Schwingenschlögl, F. Laquai, S. D. Wolf, *Science* **2022**, *377*, 302.

[52] X. Y. Chin, D. Turkay, J. A. Steele, S. Tabean, S. Eswara, M. Mensi, P. Fiala, C. M. Wolff, A. Paracchino, K. Artuk, D. Jacobs, Q. Guesnay, F. Sahli, G. Andreatta, M. Boccard, Q. Jeangros, C. Ballif, *Science* **2023**, *381*, 59.

[53] S. Mariotti, E. Köhnen, F. Scheler, K. Sveinbjörnsson, L. Zimmermann, M. Piot, F. Yang, B. Li, J. Warby, A. Musiienko, D. Menzel, F. Lang, S. Keßler, I. Levine, D. Mantione, A. Al-Ashouri, M. S. Härtel, K. Xu, A. Cruz, J. Kurpiers, P. Wagner, H. Köbler, J. Li, A. Magomedov, D. Mecerreyes, E. Unger, A. Abate, M. Stolterfoht, B. Stannowski, R. Schlatmann, et al., *Science* **2023**, *381*, 63.

[54] A. Al-Ashouri, A. Magomedov, M. Roß, M. Jošt, M. Talaikis, G. Chistiakova, T. Bertram, J. A. Márquez, E. Köhnen, E. Kasparavičius, S. Levcenco, L. Gil-Escrig, C. J. Hages, R. Schlatmann, B. Rech, T. Malinauskas, T. Unold, C. A. Kaufmann, L. Korte, G. Niaura, V. Getautis, S. Albrecht, *Energy Environ. Sci.* **2019**, *12*, 3356.

[55] Q. Han, Y.-T. Hsieh, L. Meng, J.-L. Wu, P. Sun, E.-P. Yao, S.-Y. Chang, S.-H. Bae, T. Kato, V. Bermudez, Y. Yang, *Science* **2018**, *361*, 904.

[56] M. Jošt, E. Köhnen, A. Al-Ashouri, T. Bertram, Š. Tomšič, A. Magomedov, E. Kasparavicius, T. Kodalle, B. Lipovšek, V. Getautis,

R. Schlatmann, C. A. Kaufmann, S. Albrecht, M. Topič, *ACS Energy Lett.* **2022**, *7*, 1298.

[57] K. O. Brinkmann, T. Becker, F. Zimmermann, C. Kreusel, T. Gahlmann, M. Theisen, T. Haeger, S. Olthof, C. Tuckmantel, M. Gunster, T. Maschwitz, F. Gobelsmann, C. Koch, D. Hertel, P. Caprioglio, F. Pena-Camargo, L. Perdigon-Toro, A. Al-Ashouri, L. Merten, A. Hinderhofer, L. Gomell, S. Zhang, F. Schreiber, S. Albrecht, K. Meerholz, D. Neher, M. Stolterfoht, T. Riedl, *Nature* **2022**, *604*, 280.

[58] W. Chen, Y. Zhu, J. Xiu, G. Chen, H. Liang, S. Liu, H. Xue, E. Birgersson, J. W. Ho, X. Qin, J. Lin, R. Ma, T. Liu, Y. He, A. M.-C. Ng, X. Guo, Z. He, H. Yan, A. B. Djurišić, Y. Hou, *Nat. Energy* **2022**, *7*, 229.

[59] Y. Ogomi, A. Morita, S. Tsukamoto, T. Saitho, N. Fujikawa, Q. Shen, T. Toyoda, K. Yoshino, S. S. Pandey, T. Ma, S. Hayase, *J. Phys. Chem. Lett.* **2014**, *5*, 1004.

[60] A. Goyal, S. McKechnie, D. Pashov, W. Tumas, M. van Schilfgaarde, V. Stevanović, *Chem. Mater.* **2018**, *30*, 3920.

[61] E. S. Parrott, T. Green, R. L. Milot, M. B. Johnston, H. J. Snaith, L. M. Herz, *Adv. Funct. Mater.* **2018**, *28*, 1802803.

[62] A. Rajagopal, R. J. Stoddard, H. W. Hillhouse, A. K. Y. Jen, *J. Mater. Chem. A* **2019**, *7*, 16285.

[63] I. Chung, J. H. Song, J. Im, J. Androulakis, C. D. Malliakas, H. Li, A. J. Freeman, J. T. Kenney, M. G. Kanatzidis, *J. Am. Chem. Soc.* **2012**, *134*, 8579.

[64] F. Hao, C. C. Stoumpos, D. H. Cao, R. P. H. Chang, M. G. Kanatzidis, *Nat. Photonics* **2014**, *8*, 489.

[65] J. Pascual, G. Nasti, M. H. Aldamasy, J. A. Smith, M. Flatken, N. Phung, D. Di Girolamo, S.-H. Turren-Cruz, M. Li, A. Dallmann, R. Avolio, A. Abate, *Mater. Adv.* **2020**, *1*, 1066.

[66] M. I. Saidaminov, I. Spanopoulos, J. Abed, W. Ke, J. Wicks, M. G. Kanatzidis, E. H. Sargent, *ACS Energy Lett.* **2020**, *5*, 1153.

[67] Z. Zhang, J. Liang, J. Wang, Y. Zheng, X. Wu, C. Tian, A. Sun, Y. Huang, Z. Zhou, Y. Yang, Y. Liu, C. Tang, C. C. Chen, *Adv. Energy Mater.* **2023**, *13*, 2300181.

[68] M. H. Du, *J. Mater. Chem. A* **2014**, *2*, 9091.

[69] W. Gao, C. Chen, C. Ran, H. Zheng, H. Dong, Y. Xia, Y. Chen, W. Huang, *Adv. Funct. Mater.* **2020**, *30*, 2000794.

[70] T. Leijtens, R. Prasanna, A. Gold-Parker, M. F. Toney, M. D. McGehee, *ACS Energy Lett.* **2017**, *2*, 2159.

[71] C. Ran, J. Xu, W. Gao, C. Huang, S. Dou, *Chem. Soc. Rev.* **2018**, *47*, 4581.

[72] M. T. Klug, R. L. Milot, J. B. Patel, T. Green, H. C. Sansom, M. D. Farrar, A. J. Ramadan, S. Martani, Z. Wang, B. Wenger, J. M. Ball, L. Langshaw, A. Petrozza, M. B. Johnston, L. M. Herz, H. J. Snaith, *Energy Environ. Sci.* **2020**, *13*, 1776.

[73] F. Hao, C. C. Stoumpos, P. Guo, N. Zhou, T. J. Marks, R. P. Chang, M. G. Kanatzidis, *J. Am. Chem. Soc.* **2015**, *137*, 11445.

[74] E. Jokar, C.-H. Chien, A. Fathi, M. Rameez, Y.-H. Chang, E. W.-G. Diau, *Energy Environ. Sci.* **2018**, *11*, 2353.

[75] F. Yang, J. Liu, X. Wang, K. Tanaka, K. Shinokita, Y. Miyauchi, A. Wakamiya, K. Matsuda, *ACS Appl. Mater. Interfaces* **2019**, *11*, 15680.

[76] J. Liu, G. Wang, Z. Song, X. He, K. Luo, Q. Ye, C. Liao, J. Mei, *J. Mater. Chem. A* **2017**, *5*, 9097.

[77] Z. Yang, A. Rajagopal, A. K. Jen, *Adv. Mater.* **2017**, *29*, 1704418.

[78] Y. M. Lee, J. Park, B. D. Yu, S. Hong, M. C. Jung, M. Nakamura, *J. Phys. Chem. Lett.* **2018**, *9*, 2293.

[79] W. F. Yang, F. Igbari, Y. H. Lou, Z. K. Wang, L. S. Liao, *Adv. Energy Mater.* **2019**, *10*, 1902584.

[80] Q. Shen, Y. Ogomi, J. Chang, T. Toyoda, K. Fujiwara, K. Yoshino, K. Sato, K. Yamazaki, M. Akimoto, Y. Kuga, K. Katayama, S. Hayase, *J. Mater. Chem. A* **2015**, *3*, 9308.

[81] J. H. Heo, H. J. Han, D. Kim, T. K. Ahn, S. H. Im, *Energy Environ. Sci.* **2015**, *8*, 1602.

[82] P. Lopez-Varo, J. A. Jiménez-Tejada, M. García-Rosell, S. Ravishankar, G. Garcia-Belmonte, J. Bisquert, O. Almora, *Adv. Energy Mater.* **2018**, *8*, 1702772.

[83] B. Chen, M. Yang, S. Priya, K. Zhu, *J. Phys. Chem. Lett.* **2016**, *7*, 905.

[84] S. J. Lee, S. S. Shin, Y. C. Kim, D. Kim, T. K. Ahn, J. H. Noh, J. Seo, S. I. Seok, *J. Am. Chem. Soc.* **2016**, *138*, 3974.

[85] W. Liao, D. Zhao, Y. Yu, C. R. Grice, C. Wang, A. J. Cimaroli, P. Schulz, W. Meng, K. Zhu, R. G. Xiong, Y. Yan, *Adv. Mater.* **2016**, *28*, 9333.

[86] D. Moghe, L. Wang, C. J. Traverse, A. Redoute, M. Sponseller, P. R. Brown, V. Bulović, R. R. Lunt, *Nano Energy* **2016**, *28*, 469.

[87] M. H. Kumar, S. Dharani, W. L. Leong, P. P. Boix, R. R. Prabhakar, T. Baikie, C. Shi, H. Ding, R. Ramesh, M. Asta, M. Graetzel, S. G. Mhaisalkar, N. Mathews, *Adv. Mater.* **2014**, *26*, 7122.

[88] W. Ke, C. C. Stoumpos, I. Spanopoulos, L. Mao, M. Chen, M. R. Wasielewski, M. G. Kanatzidis, *J. Am. Chem. Soc.* **2017**, *139*, 14800.

[89] W. Ke, C. C. Stoumpos, M. Zhu, L. Mao, I. Spanopoulos, J. Liu, O. Y. Kontsevoi, M. Chen, D. Sarma, Y. Zhang, M. R. Wasielewski, M. G. Kanatzidis, *Sci. Adv.* **2017**, *3*, e1701293.

[90] W. Ke, C. C. Stoumpos, M. G. Kanatzidis, *Adv. Mater.* **2019**, *31*, 1803230.

[91] F. Wu, R. Pathak, K. Chen, G. Wang, B. Bahrami, W.-H. Zhang, Q. Qiao, *ACS Energy Lett.* **2018**, *3*, 2457.

[92] E. W.-G. Diau, E. Jokar, M. Rameez, *ACS Energy Lett.* **2019**, *4*, 1930.

[93] G. Kapil, T. Bessho, C. H. Ng, K. Hamada, M. Pandey, M. A. Kamarudin, D. Hirotani, T. Kinoshita, T. Minemoto, Q. Shen, T. Toyoda, T. N. Murakami, H. Segawa, S. Hayase, *ACS Energy Lett.* **2019**, *4*, 1991.

[94] T. S. Ripolles, D. Yamasuso, Y. Zhang, M. A. Kamarudin, C. Ding, D. Hirotani, Q. Shen, S. Hayase, *J. Phys. Chem. C* **2018**, *122*, 27284.

[95] Y. Zong, Z. Zhou, M. Chen, N. P. Padture, Y. Zhou, *Adv. Energy Mater.* **2018**, *8*, 1800997.

[96] J. Tong, J. Gong, M. Hu, S. K. Yadavalli, Z. Dai, F. Zhang, C. Xiao, J. Hao, M. Yang, M. A. Anderson, E. L. Ratcliff, J. J. Berry, N. P. Padture, Y. Zhou, K. Zhu, *Matter* **2021**, *4*, 1365.

[97] A. R. Bowman, M. T. Klug, T. A. S. Doherty, M. D. Farrar, S. P. Senanayak, B. Wenger, G. Divitini, E. P. Booker, Z. Andaji-Garmaroudi, S. Macpherson, E. Ruggeri, H. Sirringhaus, H. J. Snaith, S. D. Stranks, *ACS Energy Lett.* **2019**, *4*, 2301.

[98] S. R. Sahamir, M. A. Kamarudin, T. S. Ripolles, A. K. Baranwal, G. Kapil, Q. Shen, H. Segawa, J. Bisquert, S. Hayase, *J. Phys. Chem. Lett.* **2022**, *13*, 3130.

[99] W. Liao, D. Zhao, Y. Yu, N. Shrestha, K. Ghimire, C. R. Grice, C. Wang, Y. Xiao, A. J. Cimaroli, R. J. Ellingson, N. J. Podraza, K. Zhu, R. G. Xiong, Y. Yan, *J. Am. Chem. Soc.* **2016**, *138*, 12360.

[100] Q. Chen, J. Wu, J. T. Matondo, L. Bai, D. M. Maurice, M. Guli, *Sol. RRL* **2020**, *4*, 2000584.

[101] X. Lian, J. Chen, Y. Zhang, M. Qin, J. Li, S. Tian, W. Yang, X. Lu, G. Wu, H. Chen, *Adv. Funct. Mater.* **2018**, *29*, 1807024.

[102] C. Li, Y. Pan, J. Hu, S. Qiu, C. Zhang, Y. Yang, S. Chen, X. Liu, C. J. Brabec, M. K. Nazeeruddin, Y. Mai, F. Guo, *ACS Energy Lett.* **2020**, *5*, 1386.

[103] W. Ke, C. Chen, I. Spanopoulos, L. Mao, I. Hadar, X. Li, J. M. Hoffman, Z. Song, Y. Yan, M. G. Kanatzidis, *J. Am. Chem. Soc.* **2020**, *142*, 15049.

[104] M. Liu, N. Yazdani, M. Yarema, M. Jansen, V. Wood, E. H. Sargent, *Nat. Electron.* **2021**, *4*, 548.

[105] H. Zheng, W. Wu, H. Xu, F. Zheng, G. Liu, X. Pan, Q. Chen, *Adv. Funct. Mater.* **2020**, *30*, 2000034.

[106] X. Xu, C.-C. Chueh, Z. Yang, A. Rajagopal, J. Xu, S. B. Jo, A. K. Y. Jen, *Nano Energy* **2017**, *34*, 392.

[107] S. Zhou, S. Fu, C. Wang, W. Meng, J. Zhou, Y. Zou, Q. Lin, L. Huang, W. Zhang, G. Zeng, D. Pu, H. Guan, C. Wang, K. Dong, H. Cui, S. Wang, T. Wang, G. Fang, W. Ke, *Nature* **2023**, *624*, 69.

**ADVANCED
SCIENCE NEWS**

www.advancedsciencenews.com

**ADVANCED
MATERIALS**

www.advmat.de

[108] W. Yan, C. Li, C. Peng, S. Tan, J. Zhang, H. Jiang, F. Xin, F. Yue, Z. Zhou, *Adv. Mater.* **2024**, *36*, 2312170.

[109] D. Di Girolamo, J. Pascual, M. H. Aldamasy, Z. Iqbal, G. Li, E. Radicchi, M. Li, S.-H. Turren-Cruz, G. Nasti, A. Dallmann, F. De Angelis, A. Abate, *ACS Energy Lett.* **2021**, *6*, 959.

[110] K. D. G. I. Jayawardena, R. M. I. Bandara, M. Monti, E. Butler-Caddle, T. Pichler, H. Shiozawa, Z. Wang, S. Jenatsch, S. J. Hinder, M. G. Masteghin, M. Patel, H. M. Thirimanne, W. Zhang, R. A. Sporea, J. Lloyd-Hughes, S. R. P. Silva, *J. Mater. Chem. A* **2020**, *8*, 693.

[111] L. Zeng, Z. Chen, S. Qiu, J. Hu, C. Li, X. Liu, G. Liang, C. J. Brabec, Y. Mai, F. Guo, *Nano Energy* **2019**, *66*, 104099.

[112] M. Wei, K. Xiao, G. Walters, R. Lin, Y. Zhao, M. I. Saidaminov, P. Todorovic, A. Johnston, Z. Huang, H. Chen, A. Li, J. Zhu, Z. Yang, Y. K. Wang, A. H. Proppe, S. O. Kelley, Y. Hou, O. Voznyy, H. Tan, E. H. Sargent, *Adv. Mater.* **2020**, *32*, 1907058.

[113] S. Hu, P. Zhao, K. Nakano, R. D. J. Oliver, J. Pascual, J. A. Smith, T. Yamada, M. A. Truong, R. Murdey, N. Shioya, T. Hasegawa, M. Ehara, M. B. Johnston, K. Tajima, Y. Kanemitsu, H. J. Snaith, A. Wakamiya, *Adv. Mater.* **2023**, *35*, 2208320.

[114] G. Kapil, T. S. Ripolles, K. Hamada, Y. Ogomi, T. Bessho, T. Kinoshita, J. Chantana, K. Yoshino, Q. Shen, T. Toyoda, T. Minemoto, T. N. Murakami, H. Segawa, S. Hayase, *Nano Lett.* **2018**, *18*, 3600.

[115] G. Kapil, T. Bessho, T. Maekawa, A. K. Baranwal, Y. Zhang, M. A. Kamarudin, D. Hirotani, Q. Shen, H. Segawa, S. Hayase, *Adv. Energy Mater.* **2021**, *11*, 202101069.

[116] M. Liu, Z. Chen, Q. Xue, S. H. Cheung, S. K. So, H.-L. Yip, Y. Cao, *J. Mater. Chem. A* **2018**, *6*, 16347.

[117] B. Abdollahi Nejand, I. M. Hossain, M. Jakoby, S. Moghadamzadeh, T. Abzieher, S. Gharibzadeh, J. A. Schwenzer, P. Nazari, F. Schackmar, D. Hauschild, L. Weinhardt, U. Lemmer, B. S. Richards, I. A. Howard, U. W. Paetzold, *Adv. Energy Mater.* **2019**, *10*, 1902583.

[118] Z. Yang, B. H. Babu, S. Wu, T. Liu, S. Fang, Z. Xiong, L. Han, W. Chen, *Sol. RRL* **2019**, *4*, 1900257.

[119] G. Lin, Y. Lin, H. Huang, R. Cui, X. Guo, B. Liu, J. Dong, X. Guo, B. Sun, *Nano Energy* **2016**, *27*, 638.

[120] H. Guo, H. Zhang, S. Liu, D. Zhang, Y. Wu, W. H. Zhu, *ACS Appl. Mater. Interfaces* **2022**, *14*, 6852.

[121] H. Tang, Y. Shang, W. Zhou, Z. Peng, Z. Ning, *Sol. RRL* **2018**, *3*, 1800256.

[122] M. Zhang, D. Chi, J. Wang, F. Wu, S. Huang, *Sol. Energy* **2020**, *201*, 589.

[123] Y. Kim, E. H. Jung, G. Kim, D. Kim, B. J. Kim, J. Seo, *Adv. Energy Mater.* **2018**, *8*, 1801668.

[124] W. S. Yang, B.-W. Park, E. H. Jung, N. J. Jeon, Y. C. Kim, D. U. Lee, S. S. Shin, J. Seo, E. K. Kim, J. H. Noh, S. I. Seok, *Science* **2017**, *356*, 1376.

[125] J. H. Heo, S. H. Im, J. H. Noh, T. N. Mandal, C.-S. Lim, J. A. Chang, Y. H. Lee, H.-j. Kim, A. Sarkar, M. K. Nazeeruddin, M. Grätzel, S. I. Seok, *Nat. Photonics* **2013**, *7*, 486.

[126] Y. Wang, W. Fu, J. Yan, J. Chen, W. Yang, H. Chen, *J. Mater. Chem. A* **2018**, *6*, 13090.

[127] M. Pitaro, J. S. Alonso, L. Di Mario, D. Garcia Romero, K. Tran, T. Zaharia, M. B. Johansson, E. M. J. Johansson, M. A. Loi, *J. Mater. Chem. A* **2023**, *11*, 11755.

[128] A. R. Bowman, F. Lang, Y. H. Chiang, A. Jimenez-Solano, K. Frohna, G. E. Eperon, E. Ruggeri, M. Abdi-Jalebi, M. Anaya, B. V. Lotsch, S. D. Stranks, *ACS Energy Lett.* **2021**, *6*, 612.

[129] L. M. Herz, *ACS Energy Lett.* **2017**, *2*, 1539.

[130] J. Guo, B. Wang, D. Lu, T. Wang, T. Liu, R. Wang, X. Dong, T. Zhou, N. Zheng, Q. Fu, Z. Xie, X. Wan, G. Xing, Y. Chen, Y. Liu, *Adv. Mater.* **2023**, *35*, 2212126.

[131] Q. Jiang, R. Tirawat, R. A. Kerner, E. A. Gaulding, Y. Xian, X. Wang, J. M. Newkirk, Y. Yan, J. J. Berry, K. Zhu, *Nature* **2023**, *623*, 313.

[132] L. E. Mundt, J. Tong, A. F. Palmstrom, S. P. Dunfield, K. Zhu, J. J. Berry, L. T. Schelhas, E. L. Ratcliff, *ACS Energy Lett.* **2020**, *5*, 3344.

[133] T. Leijtens, K. A. Bush, R. Prasanna, M. D. McGehee, *Nat. Energy* **2018**, *3*, 828.

[134] J. Li, T. Jiu, S. Chen, L. Liu, Q. Yao, F. Bi, C. Zhao, Z. Wang, M. Zhao, G. Zhang, Y. Xue, F. Lu, Y. Li, *Nano Lett.* **2018**, *18*, 6941.

[135] J. Wen, Y. Zhao, Z. Liu, H. Gao, R. Lin, S. Wan, C. Ji, K. Xiao, Y. Gao, Y. Tian, J. Xie, C. J. Brabec, H. Tan, *Adv. Mater.* **2022**, *34*, 2110356.

[136] P. Wu, J. Wen, Y. Wang, Z. Liu, R. Lin, H. Li, H. Luo, H. Tan, *Adv. Energy Mater.* **2022**, *12*, 2202948.

[137] J. Ávila, C. Momblona, P. Boix, M. Sessolo, M. Anaya, G. Lozano, K. Vandewal, H. Míguez, H. J. Bolink, *Energy Environ. Sci.* **2018**, *11*, 3292.

[138] H. Lai, J. Luo, Y. Zwirner, S. Olthof, A. Wieczorek, F. Ye, Q. Jeangros, X. Yin, F. Akhundova, T. Ma, R. He, R. K. Kothandaraman, X. Chin, E. Gilshtein, A. Müller, C. Wang, J. Thiesbrummel, S. Siol, J. M. Prieto, T. Unold, M. Stolterfoht, C. Chen, A. N. Tiwari, D. Zhao, F. Fu, *Adv. Energy Mater.* **2022**, *12*, 2202438.

[139] J. Luo, R. He, H. Lai, C. Chen, J. Zhu, Y. Xu, F. Yao, T. Ma, Y. Luo, Z. Yi, Y. Jiang, Z. Gao, J. Wang, W. Wang, H. Huang, Y. Wang, S. Ren, Q. Lin, C. Wang, F. Fu, D. Zhao, *Adv. Mater.* **2023**, *35*, 2300352.

[140] J. Zhu, Y. Luo, R. He, C. Chen, Y. Wang, J. Luo, Z. Yi, J. Thiesbrummel, C. Wang, F. Lang, H. Lai, Y. Xu, J. Wang, Z. Zhang, W. Liang, G. Cui, S. Ren, X. Hao, H. Huang, Y. Wang, F. Yao, Q. Lin, L. Wu, J. Zhang, M. Stolterfoht, F. Fu, D. Zhao, *Nat. Energy* **2023**, *8*, 714.

[141] B. Abdollahi Nejand, D. B. Ritzer, H. Hu, F. Schackmar, S. Moghadamzadeh, T. Feeney, R. Singh, F. Laufer, R. Schmager, R. Azmi, M. Kaiser, T. Abzieher, S. Gharibzadeh, E. Ahlswede, U. Lemmer, B. S. Richards, U. W. Paetzold, *Nat. Energy* **2022**, *7*, 620.

[142] Z. Yu, X. Chen, S. P. Harvey, Z. Ni, B. Chen, S. Chen, C. Yao, X. Xiao, S. Xu, G. Yang, Y. Yan, J. J. Berry, M. C. Beard, J. Huang, *Adv. Mater.* **2022**, *34*, 2110351.

[143] F. Yang, P. Tockhorn, A. Musiienko, F. Lang, D. Menzel, R. Macqueen, E. Kohnen, K. Xu, S. Mariotti, D. Mantione, L. Merten, A. Hinderhofer, B. Li, D. R. Wargulski, S. P. Harvey, J. Zhang, F. Scheler, S. Berwig, M. Ross, J. Thiesbrummel, A. Al-Ashouri, K. O. Brinkmann, T. Riedl, F. Schreiber, D. Abou-Ras, H. Snaith, D. Neher, L. Korte, M. Stolterfoht, S. Albrecht, *Adv. Mater.* **2024**, *36*, 2307743.

[144] K. Xiao, Y.-H. Lin, M. Zhang, R. D. J. Oliver, X. Wang, Z. Liu, X. Luo, J. Li, D. Lai, H. Luo, R. Lin, J. Xu, Y. Hou, H. J. Snaith, H. Tan, *Science* **2022**, *376*, 762.

[145] Q. Jiang, J. Tong, R. A. Scheidt, X. Wang, A. E. Louks, Y. Xian, R. Tirawat, A. F. Palmstrom, M. P. Hautzinger, S. P. Harvey, S. Johnston, L. T. Schelhas, B. W. Larson, E. L. Warren, M. C. Beard, J. J. Berry, Y. Yan, K. Zhu, *Science* **2022**, *378*, 1295.

[146] F. Peña-Camargo, P. Caprioglio, F. Zu, E. Gutierrez-Partida, C. M. Wolff, K. Brinkmann, S. Albrecht, T. Riedl, N. Koch, D. Neher, M. Stolterfoht, *ACS Energy Lett.* **2020**, *5*, 2728.

**ADVANCED
SCIENCE NEWS**

www.advancedsciencenews.com

**ADVANCED
MATERIALS**

www.advmat.de

Fengjiu Yang is a researcher in the Chemistry and Nanoscience Science Center at the National Renewable Energy Laboratory (NREL). He received his Ph.D. degree in Energy Science from Kyoto University under the supervision of Prof. Kazunari Matsuda and Prof. Atsushi Wakamiya in 2019. His research interests include the development and design of perovskite-based photovoltaics (perovskite single junction solar cells, all-perovskite monolithic tandems, and perovskite-Si monolithic tandems), carrier charge transport materials and carrier extraction mechanisms, interface recombination losses and treatment engineering, photovoltaics stability operation, and quantum dots materials.

Kai Zhu is currently a principal scientist in the Chemistry and Nanoscience Science Center at the National Renewable Energy Laboratory (NREL). He received his Ph.D. degree in Physics from Syracuse University in 2003. His research interests have included characterization and modeling of hydrogenated amorphous silicon thin film solar cell, III–V wide-bandgap light emitting diodes, dye-sensitized solar cells, and Li-ion batteries and supercapacitors. His current research focuses on perovskite solar cells, including material development, device fabrication, and fundamental characterization of charge-carrier dynamics and device operating principles.

2314341 (21 of 21)